RSC Advances

PAPER

View Article Online
View Journal | View Issue

Cite this: *RSC Adv.*, 2025, **15**, 10049

From waste to energy storage: fabrication of shape-stabilized phase change composites using cellulose extracted from waste paper

Sahel Saberi,[a] Golnoosh Abdeali*[bc] and Ahmad Reza Bahramian *[a]

Organic phase change materials (PCMs) are promising for sustainable energy due to their high storage capacity, broad temperature control, and minimal volume change during phase transitions. However, their application is limited by low thermal conductivity and high leakage caused by volume instability. To address these issues, a shape-stabilizing approach using a nature-based and porous matrix of cellulose from recyclable resources, is proposed. In this study, a cellulose hydrogel-based composite was used as a support for encapsulating polyethylene glycol (PEG 2000) PCM, creating a phase change composite (PCC). Cellulose was extracted from waste newspaper (WP) through alkaline and peroxide treatments, achieving 16.5% efficiency and 78% purity. The cellulose was then used to synthesize different three-dimensional (3D) hydrogel networks with citric acid (CA) as the cross-linking agent. Carbon monofilaments (CFs) were incorporated into the hydrogels to enhance stability, reduce leakage, and improve thermal properties. The thermophysical and morphological characterization of the prepared system revealed that cellulose-based hydrogels were formed through esterification between cellulose hydroxyl groups and CA carboxyl groups. The leakage rate of the (cell-4/CF/PEG) PCC was measured as 4.25 wt% after 5 heating–cooling cycles. The latent heat of melting was similar to pure PEG 2000, with an energy storage capacity increase of 25%. Furthermore, the addition of CFs improved thermal conductivity (k) by 80% and achieved an enthalpy efficiency of 90%. The thermal diffusivity (α), specific heat capacity (C_p), and effective thermal conductivity (k_{eff}) of the (cell-4/CF/PEG) PCC were recorded as 8.2×10^{-9} m^2 s^{-1}, 5400 J kg^{-1} °C^{-1}, and 0.027 W m^{-1} °C^{-1}, respectively.

Received 7th November 2024
Accepted 4th March 2025

DOI: 10.1039/d4ra07932a

rsc.li/rsc-advances

1. Introduction

In the past decades, thermal energy storage (TES) has enabled heat transfer to different substrates during the storage cycle and release during the discharge phase.[1] Latent heat energy storage (LHES) is a suitable TES method, offering high storage density with a low temperature difference between storage and heat release.[2,3] Phase change materials (PCMs) store and release thermal energy as the latent heat without temperature change during the phase change (*e.g.*, solid–liquid).[4] The latent heat of melting and crystallization allows PCMs to store more heat than other heat storage mechanisms (*e.g.*, sensible and chemical reactions).[1] Organic PCMs like polyethylene glycol (PEG) are ideal for clean energy conversion/storage due to their wide temperature range, high fusion latent heat, compatibility with other materials, durability, non-toxicity, and low cost.[2,4] Additionally, they are suitable for long-term energy storage due to their high thermal stability, preventing degradation over time.[1,5] However, PCMs face challenges such as the super-cooling effect, low thermal conductivity, and poor structural stability, reducing heat transfer efficiency and causing liquid phase leakage.[4] Efforts to tackle these challenges include PCM encapsulation through shape-stabilizing (SS-PCM) methods like melt infiltration, impregnation, and sol–gel[3] using porous structures like hydrogels.[6]

Hydrogels, with their porous 3-dimensional networks, offer excellent mechanical and thermophysical properties. A sustainable method to fabricate hydrogels involves using waste paper (WP). The extensive global use of the pulp and paper industry has led to the annual production of a huge amount of WP, which contains natural polymers such as cellulose (40–55%), hemicellulose (25–40%) and lignin (18–30%).[7] Fabrication of cellulose-based hydrogels using WP, can ultimately lead to the final product's biocompatibility, cost and environmental pollution reduction, as well as originating from renewable sources.[8,9] Due to the use of renewable resources and potential to reduce environmental challenges, the cellulosic hydrogel for the phase change composite (PCC) was made using the cellulose extracted from WP as the starting material in this study.

[a]*Polymer Engineering Department, Faculty of Chemical Engineering, Tarbiat Modares University, P. O. Box 14115-143, Tehran, Iran. E-mail: abahramian@modares.ac.ir*
[b]*PRISM Research Institute, Technological University of the Shannon, University Road, N37HD68 Athlone, Ireland. E-mail: golnoosh.abdeali@tus.ie*
[c]*Applied Polymer Technologies Gateway, Technological University of the Shannon: Midlands Midwest, Athlone Campus, University Road, N37HD68 Athlone, Ireland*

Table 1 Recent studies on cellulose extraction from various sources for different applications

Cellulose source	Treatments	Solvent	Cross-linking agent/method	Synthesis results	Application	Reference
Cassava peel	(A) Nitric method: NH_3 3.5%, NaOH 2%, $NaSO_3$ 2%, $NaClO_2$ 2% (B) Sulfuric method: H_2SO_4 0.5 M, $NaClO_2$ 2% (C) Alkaline method: NaOH 4%, NaClO 4%	—	—	The alkaline method had the highest yield (17.80%) and cellulose content (93.24%), with type II cellulose and a 51% crystallinity index	—	12
Sugarcane bagasse	(A) Hemicellulose removal: H_2SO_4 10% (v/v)	NaOH : urea (aq.) (7 : 12)	CA, ECH/freeze-thawing (−20, 30 °C)	The final pulp contained 84% cellulose, 12% hemicellulose and lignin, and 4% water. Adding 40% CA formed a hydrogel with mechanical strength similar to one cross-linked with 5% ECH	Methylene blue dye removal	13
	(B) Delignification: NaOH 20% (w/v)			Crystallinity analysis showed cellulose I and II in both hydrogels, with crystallinity indices of 49% for CA and 54% for ECH		
	(C) Bleaching: NaClO 1% (v/v)			Porosity measurements indicated higher porosity in the CA-cross-linked hydrogel		
Starch	—	Water	CA/heating (70–80, 105 °C)	With an increase in the content of CA as a cross-linker, the swelling degree of hydrogels drops. The highest swelling degree is 8.55 for the hydrogel with the smallest content of CA	Drug delivery	14
Rice husk	(A) HNO_3 1 M (B) NaOH 1 M (24 h), NaOH 6 M (6 h) (C) H_2SO_4 5 M (up to pH = 5–6)	—	—	The cellulose extraction rate was 17.4%	—	7
WP	(A) Alkaline treatment: NaOH 20% (70 °C, 2 h) (B) Bleaching: H_2O_2 1.5% (70 °C, 1 h)	NaOH : urea (aq.) (7 : 12)	CA/heating (30–70 °C)	As temperature increases, the swelling ratio decreases initially and then increases. At low temperatures, less cross-links form, while at higher temperatures, stronger hydrogen bonds between CA and cellulose improve water stability	Agricultural medium	11

However, cellulose-based hydrogels extracted from WP have inadequate mechanical properties which can be improved by cross-linking their structure. Conventional synthetic cross-linkers like epichlorohydrin (ECH) and formaldehyde have disadvantages including high toxicity, low biodegradability, poor biocompatibility, and low aqueous solubility.[10] To address these complexities, novel cross-linking agents like polyfunctional carboxylic acids (such as CA) have been introduced, resulting in biodegradable hydrogel microstructures with preferred physio-chemical properties.[8,9] Hasan *et al.*[7] extracted cellulose from WP using alkaline treatment with sodium hydroxide (NaOH 7.5%) and acidic treatment with sulfuric acid (H_2SO_4 5 M), achieving a 20% extraction rate and confirming the removal of lignin and hemicellulose. Zainal *et al.*[11] fabricated cellulose-based hydrogels from WP using alkaline treatment (NaOH 20%) and hydrogen peroxide (H_2O_2 1.5%) as a bleaching agent followed by the addition of a cross-linking agent (CA) and high-temperature treatment. This process formed strong hydrogen bonds between CA and the extracted cellulose, leading to improved water retention. Table 1 summarizes recent studies on cellulose extraction from various sources for different applications.

Porous shape-stabilized PCMs (SS-PCMs) are commonly synthesized by impregnating molten PCMs into pre-synthesized porous support matrices of hydrogels *via* a two-step technique[6] in a way that, PCM and the porous structure interact through hydrogen bonds due to the capillary effect and surface tension, stabilizing the molten PCM within the porous microstructure. This decreases leakage during the phase change and prevents supercooling.[2,8] Khadiran *et al.*[15] shape-stabilized PEG (molecular weight of 4000 g mol^{-1}) using cellulose, agarose, and chitosan *via* solution casting. The enthalpy values for the PEG/cellulose, PEG/agarose, and PEG/chitosan phase change composites (PCCs) were lower than theoretical values due to strong hydrogen intermolecular interactions between PEG and the natural polymers, distorting PEG's crystal structure. Physical blending has been used to create shape-stabilized PCCs of PEG/cellulose, however, the supporting structure did not positively affect thermal conductivity.[16,17] It has been shown that, incorporating conductive fillers like graphite fibers,[3] carbon nanotubes (CNTs),[18] and carbon fibers (CFs)[16] can significantly increase the thermal conductivity of SS-PCMs (*e.g.*, 264% with 20 wt% graphite, almost 600% with 20 wt% CNTs, and 64.70% with 20 wt% CFs) as they can potentially minimize supercooling

Table 2 Recent studies focused on enhancing PCM performance using supporting structures

Support	PCM	Details	Results	Application	Reference
Graphene nanoplatelets/ cellulose aerogel	PEG 6000	Freeze-drying/(−55 °C) and impregnation under vacuum/(80 °C, 24 h)	The fabricated aerogel had a density of 0.06–0.12 g cm^{-3} with 89–95% open units Morphological analysis showed no clear interface between the aerogel network and PEG in the composite, indicating good compatibility, which enhanced thermal conductivity, mechanical properties, and shape stability (up to 100 °C) Thermal conductivity increased with higher graphite content, while graphite fillers reduced PCM's melting enthalpy by disrupting molecular bonding	Thermal energy storage (TES)	20
Crystalline nanocellulose	PEG 2000	Radical polymerization/ (80 °C, 4–16 h)	The composite samples maintained thermal and shape stability up to 300 °C for 120 cycles, with lower enthalpy and minimal leakage compared to pure PCM	Smart heat storage	21
Novolac/carbon monofilament/ zinc borate aerogel	Paraffin wax (PW)	Sol–gel polymerization/ (120 °C, 5 h) and impregnation/(120 °C, 48 h)	The addition of conductive fillers and zinc borate increased aerogel porosity while enhancing thermal conductivity Higher zinc borate content reduced polarity and compatibility with PW, decreasing impregnation AC0Z0 (75 wt% PW) showed no leakage, while nanocomposite aerogels (77 wt% PW) had minimal leakage, even after 10 heating–cooling cycles. Leakage below 2.59 wt% confirmed effective PW impregnation and retention	Free cooling in electrical industry	16

effect and can create a continuous path of heat transfer within the PCMs structure.[19] Yang *et al.*[20] used graphene nanoplatelets/cellulose aerogels (cellulose/GNPs) as the support structure for PEG 6000 CM to create shape-stabilized PCCs. The aerogels were synthesized *via* freeze-drying at −55 °C with ECH as the cross-linking agent, and the PCCs were produced by impregnation under vacuum at 80 °C for 24 hours. The fabricated aerogels had a density of 0.06–0.12 g cm^{-3} and 89–95% open pore cells. SEM results indicated good compatibility between the aerogel network and PEG, enhancing thermal conductivity and mechanical properties. Thermal analysis showed no weight loss until 200 °C, indicating stability within the phase change temperature range. Thermal conductivity and diffusivity improved with increased GNP content, enhancing heat transfer efficiency. It was observed that the presence of GNP fillers reduced the melting enthalpy (ΔH_{fus}) of PCM, disrupting molecular bonding and preventing crystallization. Unlike pure PEG, which melts completely at 70 °C, the fabricated composites retained their shape up to 100 °C due to the 3-dimensional network of cellulose/GNP aerogels. In addition, Table 2 summarizes recent studies primarily focused on enhancing PCM performance using supporting structures.

In this research, to improve the shape stability of PEG 2000 as the PCM and reduce leakage during the phase change, a novel surface-modified cellulose-based hydrogel extracted from WP was utilized as the shape-stabilization matrix. Furthermore, to increase the thermal conductivity and efficiency of the prepared PCM/cellulose-based hydrogel, conductive CF nanoparticles were incorporated within the hydrogel structure to benefit from their synergistic effect. The effect of CFs on the heat transfer and structural characteristics of the cellulose-based hydrogel, as well as the relationship between hydrogel microstructure (density and porosity) and the leakage behavior of the utilized PCM, were investigated. Ultimately, thermophysical models were utilized to predict the thermal characteristics of the fabricated system, including thermal diffusivity, specific heat capacity, and thermal conductivity coefficient, providing insights into its potential applications.

2. Experimental

2.1. Materials

Waste paper (WP, newspaper, purchased from local supplier), sodium hydroxide flakes (NaOH, chemical agent to remove hemicellulose, lignin and as the solvent for cellulose dissolution, Laboratory USP reagent purity ≥ 95%, Neutron Co., Iran), hydrogen peroxide (H_2O_2, concentration of 35%, delignification & deinking agent, extra pure, Dr Mojallali Co., Iran), urea powder (as the solvent for cellulose, ACS reagent Ph Eur, purity ≥ 95%, Merck Co., Germany), citric acid anhydrous powder (CA, cross-linking agent, USP reagent, purity ≥ 99.5%, Dr Mojallali Co., Iran), carbon monofilament T700S (CF, thermal conductive filler, $\rho = 1800$ kg m^{-3}, $k = 9.6$ W m^{-1} $°C^{-1}$, Toray Co., Japan), acetone (CF's solvent, laboratory USP reagent, purity ≥ 99.5%, Neutron Co., Iran), polyethylene glycol granules (PEG 2000, M_w: 1900–2100 g mol^{-1}, T_m: 50–55 °C, PCM, Daejung Co., South Korea), silicone rubber AL20 (SR, to prepare hydrogel composite reference samples, PMP Co., Iran), benzoyl peroxide PMP-CA88 (curing agent, PMP Co., Iran), deionized two-times distilled water (making and/or neutralizing different solutions & purifying the extracted cellulose powder, Sabalan Co., Iran), cellophane (to cover sample during time–temperature testing, purchased from local supplier). All the materials were used without further purification.

2.2. Methods

2.2.1. Cellulose extraction from WP

2.2.1.1. Alkaline treatment. Firstly, 20 g of WP were cut to 1 cm × 1 cm and immersed in 900 g of NaOH solvent (5, 10 and 20 wt% – pH: 13–14) at 80 °C for 2 hours to bleach WP and remove hemicellulose. Next, the samples were filtered and washed with distilled water to remove the excessive NaOH and reaching neutral pH of 7. Samples in this step were labeled as (WP/NaOH-*x*), where *x* represents the concentration of NaOH solution.

2.2.1.2. Peroxide treatment. To remove the lignin and ink of the WP resulting from the previous step, samples were bleached with 900 g of 1.5 wt% and 3 wt% H_2O_2 (pH: 5–6) at 80 °C for 1 hour. Afterward, the samples were neutralized with distilled water (pH: 7), filtered and dried in an oven at 50 °C for an hour. Samples in this step were labeled as (WP/NaOH-*x*/H_2O_2-*y*), where *x* and *y* represent the concentration of NaOH and H_2O_2 solution, respectively.

2.2.1.3. Cellulose extraction. 300 g of the mixture of solvent NaOH/urea (aq.) (7 : 12 w/w%) was prepared at −5 °C and frozen at −20 °C for an hour. Then, the frozen solution was diluted with 50 g of distilled water and stirred at 23 ± 2 °C for 5 minutes. Next, 3 g of treated WP from the peroxide treatment step was added to the solvent solution and stirred at a temperature below −10 °C for 24 hours until the solution become homogeneous. Finally, the homogeneous cellulose solution was filtered to remove excess urea and was labeled as (cellulose). This method is schematically illustrated in Fig. 1(A) (phase (1)).

2.2.2. Preparation of cellulose-based hydrogels. For the preparation of cellulose-based hydrogels, 0.7, 1.5, 3.5, 10 and 22 g of CA as the cross-linking agent was added to 10 g of cellulose solution prepared in the previous step (2.2.1.3). The pH value of these samples was set to 6, 5, 4, 3 and 2, respectively. Furthermore, prepared samples were placed on a magnetic stirrer with a stirring speed of 400 rpm for 30 minutes at 23 ± 2 °C until the added CA powder was completely solved. Finally, to carry out the chemical cross-linking between cellulose and CA, the samples were placed in an oven at 85 °C. After 72 hours, hydrogels were fabricated. The samples in this step were labeled as (cell-*z*), where *z* represents the pH of the solution of sample precursor. Table 3 shows the detailed formulation of prepared cross-linked hydrogels. In addition, the production process of hydrogels is schematically illustrated in Fig. 1(A) (phase (2)). It should be noted that, the prepared hydrogel samples were not structurally stable at pH values of 2 and 3, and the hydrogel did not form at a pH value of 6, therefore, (cell-5) and (cell-4) hydrogels were selected candidates for CF incorporation.

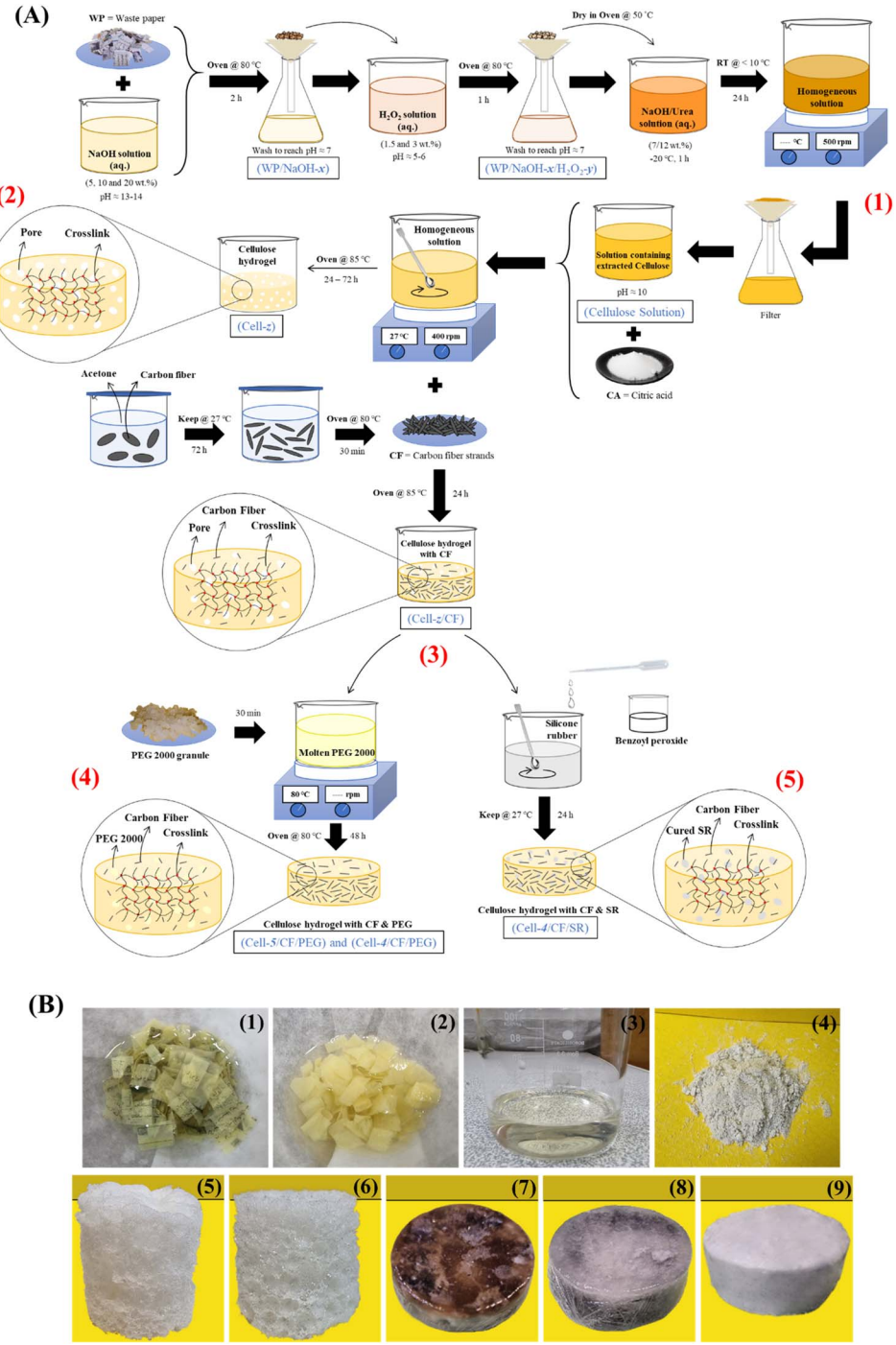

Fig. 1 (A) Sample preparation schematic: alkaline-peroxide treatment (1), hydrogel (2), hydrogel/CF (3), phase change composites (PCCs) (4) and control samples preparation (5), (B) image of WP after alkaline treatment (1), delignification and deinking (2), solvent addition (3), extracted cellulose powder (4), (cell-4) (5) and (cell-5) (6) hydrogels, (cell-4/CF/PEG) (7), (cell-5/CF/PEG) (8) and (cell-4/CF/SR) (9) systems.

2.2.3. Preparation of cellulose-based hydrogel/CF. To prepare hydrogels/CF samples, carbon monofilaments (CFs) were first cut to the length of approximately 5 mm. Furthermore, cut filaments were placed in a beaker containing 1000 mL acetone and kept at 23 ± 2 °C for 72 hours until the filaments become unwound, as a result of physical interaction with acetone. Next, the fibers were taken out of the solution and dried in an oven at 80 °C for 30 minutes. Furthermore, 1.5 g and 3.5 g of CA were added to 10 g of cellulose solution of (cell-5) and (cell-4) prepared in Section 2.2.2. Then, 0.1 g of CF was added to these solutions and stirred for 20 minutes until the both added CA and CF were well distributed in the solution. Finally, the samples were placed in an oven at 85 °C for 24 hours. The samples in this step were labeled as (cell-*z*/CF), where *z* and CF

Table 3 Detailed formulation of prepared cellulose-based cross-linked hydrogels

Sample	pH	Cellulose solution wt%	CA wt%
Cell-2	2	31.25	68.75
Cell-3	3	50.00	50.00
Cell-4	4	74.08	25.92
Cell-5	5	86.95	13.05
Cell-6	6	93.46	6.54

Table 4 Formulations of the prepared hydrogel/CFs samples

Sample	pH	Cellulose solution wt%	CA wt%	CF wt%
Cell-4/CF	4	73.53	25.73	0.74
Cell-5/CF	5	86.20	12.93	0.87

Table 5 (Cell-5/CF/PEG) and (cell-4/CF/PEG) phase change composites (PCCs) formulations

Sample	pH	Cell-z^a wt%	CF wt%	PEG 2000 wt%
Cell-4/CF/PEG	4	35.04	0.75	64.21
Cell-5/CF/PEG	5	21.55	0.80	77.65

[a] $z = 4$, (cell-4), $z = 5$, (cell-5).

Table 6 (Cell-4/CF/SR) control sample formulation

Sample	pH	Cell-z^a wt%	CF wt%	SR wt%
Cell-4/CF/SR	4	34.85	0.75	64.40

[a] $z = 4$, (cell-4).

represent the pH value of precursor and the presence of CFs in these samples, respectively. Table 4 shows the formulation of hydrogels/CFs. The production process of hydrogels/CFs is schematically illustrated in Fig. 1(A) (phase (3)).

2.2.4. Preparation of cellulose-based phase change composites (PCCs). To prepare cellulose-based phase change composites (PCCs), 10 g of PEG 2000 granulates was melted at 80 °C for 30 minutes. Furthermore, (cell-5/CF) and (cell-4/CF) samples were immersed in a beaker containing the molten PEG 2000 in an oven at 80 °C for 48 hours. By performing the impregnation process, the molten PEG 2000 was penetrated in the pores of prepared (cell-5/CF) and (cell-4/CF) samples filled the microstructures' pores. The prepared composite samples were labeled as (cell-5/CF/PEG) and (cell-4/CF/PEG), respectively (Table 5).

2.2.5. Preparation of cellulose-based composite/silicone rubber (SR). To investigate the effect of PEG 2000 PCM on the thermal properties of fabricated cellulose-based composite, (cell-4/CF/PEG) without PEG 2000 was selected as the candidate sample. To do so, (cell-4/CF) sample was impregnated with silicone rubber (SR) and the benzoyl peroxide curing agent (5 wt%). After curing at 23 ± 2 °C for 24 hours, the prepared reference sample was labeled as (cell-4/CF/SR) (Table 6). The methods mentioned in Sections 2.2.4 and 2.2.5 are schematically illustrated in Fig. 1(A) (phases (4) and (5)). Fig. 2(B) presents images of the different fabrication stages described in Sections 2.2.1–2.2.5.

3. Characterization

Fourier transform infrared-attenuated total reflectance spectroscopy (FTIR/ATR, PerkinElmer Spectrum 10.03.06, USA) was employed to investigate the chemical composition of prepared samples. Samples' dry powders were prepared as packed discs dispersed in KBr powder. The measured wavelength was from 4000 to 400 cm^{-1} at a resolution of 2.0 cm^{-1}.

To investigate the degree of crystallinity of the extracted cellulose from WP (labeled as (cellulose)), X-ray diffraction (XRD, Philips X'pert MPD, Netherlands) test was conducted within the angle range of 5–80°, step size of 0.02° s^{-1}, under a voltage of 40 kV and a current of 40 mA with Co Kα radiation (λ = 1.54056 Å). The degree of crystallinity (% X_C) for extracted cellulose powder from WP was calculated based on eqn (1).

$$\%\ X_C = \left(\frac{A_c}{A_c + A_a}\right) \times 100 \quad (1)$$

where (A_c) and (A_a) are the areas under the crystalline peaks and the amorphous regions, respectively.

The effect of the CA cross-linking agent's concentration on the cross-link density of prepared (cell-5) and (cell-4) samples was investigated by the equilibrium swelling theory.[22] First, the mass of samples was measured and recorded as (m_1). After two days and reaching the equilibrium swelling in 80 mL of distilled water, the samples were weighed again (m_2). The difference between these two values was representative of absorbed water's mass (m_w) inside the (cell-5) and (cell-4) samples. Finally, the samples were placed at 23 ± 2 °C for 72 hours to be completely dry, and then were weighed again (m_3). Ultimately, the cross-link density (ν_c) was calculated using the Flory–Renner equation (eqn (2)).[22]

$$\nu_c = \frac{1}{2M_c} = -\frac{\left(\ln(1-\nu_p)\right) + \nu_p + \chi\nu_p^2}{2 \times \rho_p \times V_s \times \left(\sqrt[3]{\nu_p} - \frac{\nu_p}{2}\right)} \quad (2)$$

where, M_c, ρ_p, V_s, ν_p and χ are the molecular weight between cross-links, polymer density, molar volume of water (0.00001807 m^3 mol^{-1}), polymer volume fraction in equilibrium swelling and Flory–Huggins polymer–solvent interaction parameter, respectively. The value of χ for hydrogels was considered to be 0.44.[23] Moreover, ν_p was calculated by eqn (3).[22]

$$\nu_p = \frac{V_p}{V_t} \quad (3)$$

where, V_p and V_t are the (cell-5) and (cell-4) samples' volume before and after swelling, respectively.

To investigate the porosity of synthesized hydrogels of (cell-5) and (cell-4), (cell-5/CF) and (cell-4/CF) and ultimately (cell-5/CF/PEG) and (cell-4/CF/PEG), the apparent density (ρ_a) was calculated by measuring the volume and the mass of the

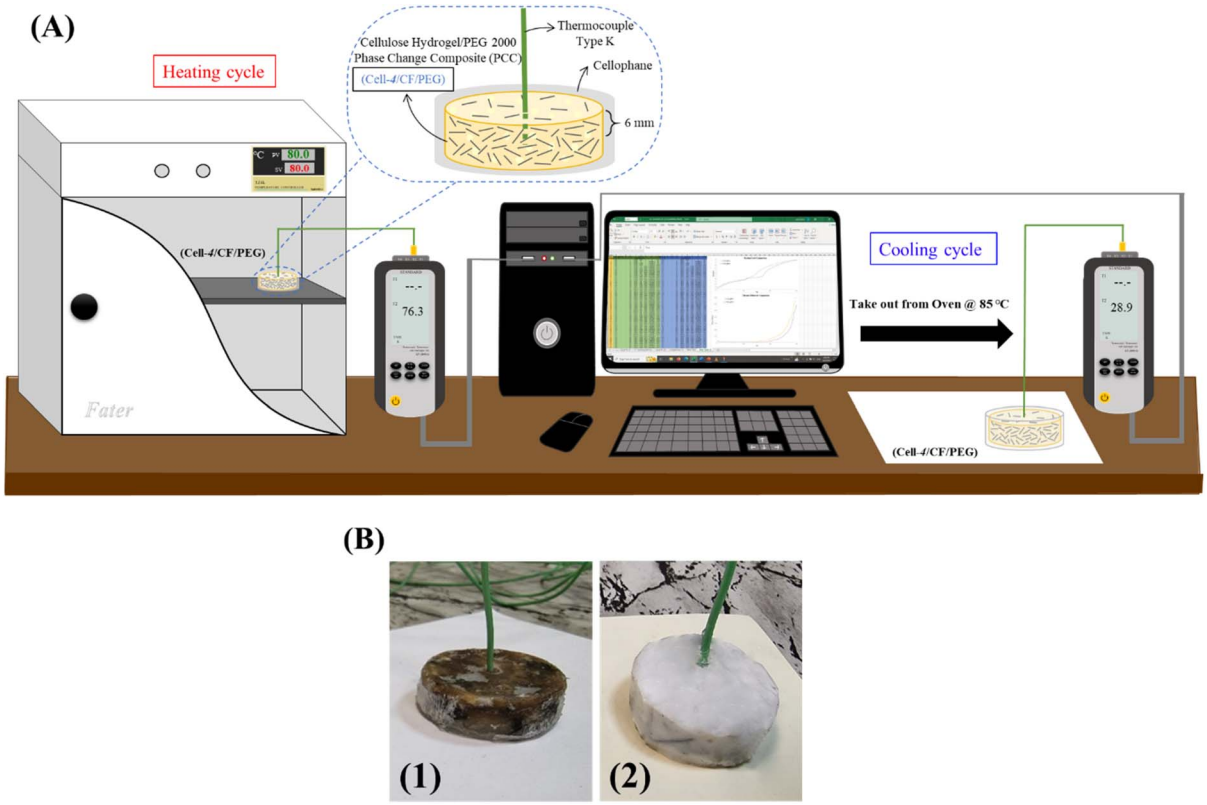

Fig. 2 Time–temperature history analysis set-up in: (A) heating and cooling cycle and (B) image of prepared (cell-4/CF/PEG) (1) and (cell-4/CF/SR) (2) samples incorporated with thermocouples.

cylindrical samples with an accuracy of 0.001 g. The theoretical density (ρ_{th}) was measured by the rule of mixtures as follows (eqn (4)):

$$\frac{1}{\rho_{th}} = \sum \frac{w_i}{\rho_i} \quad (4)$$

where, w_i and ρ_i, are the weight fraction and density of samples, respectively. Finally, the porosity ($\varepsilon_{\%}$) of the aforementioned samples was determined according to eqn (5):

$$\varepsilon_{\%} = \left(1 - \frac{\rho_a}{\rho_{th}}\right) \times 100 \quad (5)$$

To evaluate the shape stability, the leakage rate of prepared (cell-5/CF/PEG) and (cell-4/CF/PEG) composites was measured according to eqn (6). At first, samples with a primary weight of m_p were placed on a filter paper, then, they were placed in an oven at the temperature of 80 °C. After 30 minutes, samples were left in ambient temperature (23 ± 2 °C) to cool down and their mass was measured as (m_s).

$$\text{Leakage}_{\%} = \left(\frac{m_p - m_s}{m_p}\right) \times 100 \quad (6)$$

The thermal behavior and phase change characteristics of synthesized (cell-4) and (cell-4/CF/PEG) samples were investigated by differential scanning calorimetry (DSC, Q100 V9.4, TA Instruments, USA). All of the measurements were carried out under a nitrogen atmosphere at a heating/cooling rate of 10 °C min^{-1}.

Thermal performance analysis was done using time–temperature history analysis. In this test, the center of the (cell-4/CF/PEG) hydrogel composite samples were pierced for 0.625 cm, and a thermocouple (K type, Cr–Ni) with an accuracy of 0.1 °C was placed inside the punched area. During the heating cycle, the sample was placed in an oven with a temperature of 80 °C (>T_m of PEG 2000) for 2.7 hours, and during the cooling cycle, the sample was placed at 23 ± 2 °C. In both thermal cycles, the temperature recording of the sample was conducted by the digital thermometer, ST-3891G model (STANDARD Co., China). Finally, the time–temperature history results were used to calculate the thermal diffusion coefficient (α), specific heat capacity (C_p) and effective thermal conductivity coefficient (k_{eff}) of prepared (cell-4/CF/PEG) and the reference sample of (cell-4/CF/SR). Thermocouple measurement set-up are schematically illustrated in Fig. 2.

Ultimately, exploring the morphology of (cell-4) and (cell-4/CF/PEG) samples was conducted using field emission scanning electron microscopy (FESEM, Mira3 (LMU), TESCAN, Czech). The sample was coated with a thin layer of gold to improve the conductivity of the sample as well as the resolution of the pictures.

To evaluate the microstructure of the selected (cell-4) sample, pore volume, pore size distribution and specific

surface area were determined by nitrogen (N_2) adsorption–desorption porosimetry at 77 K or −196 °C (TriStar II 3020, Micromeritics, USA). The sample was degassed at 80 °C. The analysis accuracy of pore volume and specific surface area were 4×10^{-6} cm^3 g^{-1} and 0.01 m^2 g^{-1}, respectively. In addition, isotherm's measurements were done in the relative pressure range (P/P_0) of 0 to 1, by using Brunauer, Emmett and Teller (BET), Broekhoff–De Boer (BdB) and Barrett, Joyner and Halenda (BJH) theories.[24,25]

4. Results and discussion

4.1. Chemical structure characterization

The FTIR spectra of waste paper (WP), (WP/NaOH-*x*), and (WP/NaOH-*x*/H_2O_2-*y*) are shown in Fig. 3. In the FTIR spectrum of WP, broad peaks at the wavenumbers of 3394 cm^{-1} and 2933 cm^{-1} correspond to the stretching vibrations of hydroxyl groups (–OH) and C–H bonds, indicative of cellulose, hemicellulose, and lignin. The peak at the wavenumber of 1735 cm^{-1} relates to the carbonyl group (C=O) of hemicellulose.[26,27] Peaks at the wavenumbers of 1029 cm^{-1}, 1218 cm^{-1}, and 1260 cm^{-1} are attributed to C–O and C–O–C bonds related to guaiacyl and syringyl units in lignin[27–29] and further peaks at the wavenumbers of 1513 cm^{-1} and 1602 cm^{-1} represent the stretching vibrations of C=C bonds in aromatic glycosidic rings of lignin.[28,29] The C–H bending vibrations in the pyranose ring in cellulose and hemicellulose and C=O stretching in lignin appear at the wavenumbers of 1365 cm^{-1} and 1427 cm^{-1}, respectively.[27,29] In addition, asymmetrical stretching vibrations of CH_2 and CH_3 in hemicellulose and lignin are seen at the wavenumber of 2868 cm^{-1}. Finally, peaks at the wavenumbers of 662 cm^{-1}, 894 cm^{-1}, and 1318 cm^{-1} are associated with out-of-plane bending of –OH bonds, β-glycosidic linkages, and CH_2 bending in cellulose.[26,27] By comparing the FTIR spectra of WP with (WP/NaOH-5) and (WP/NaOH-10), the C=O stretching vibration band shifted to a lower wavenumber of 1706 cm^{-1} and its intensity decreased by 10%. This indicates a reduction in hemicellulose content but not complete removal for concentrations below 20 wt% NaOH as the peak at the wavenumber of 1735 cm^{-1}, which is absent in (WP/NaOH-20), confirms complete hemicellulose removal at this higher concentration.[30] Additionally, the absorption peaks in the 2800–2950 cm^{-1} and 3000–3700 cm^{-1} ranges decreased in (WP/NaOH-20), suggesting mercerization[31] due to the alkaline treatment affecting ester and hydrogen bonds.[32] In the spectrum of (WP/NaOH-20/H_2O_2-1.5) and (WP/NaOH-20/H_2O_2-3), the characteristic peaks for C–O, C–O–C, C=O, and C=C bonds in lignin are not observed in

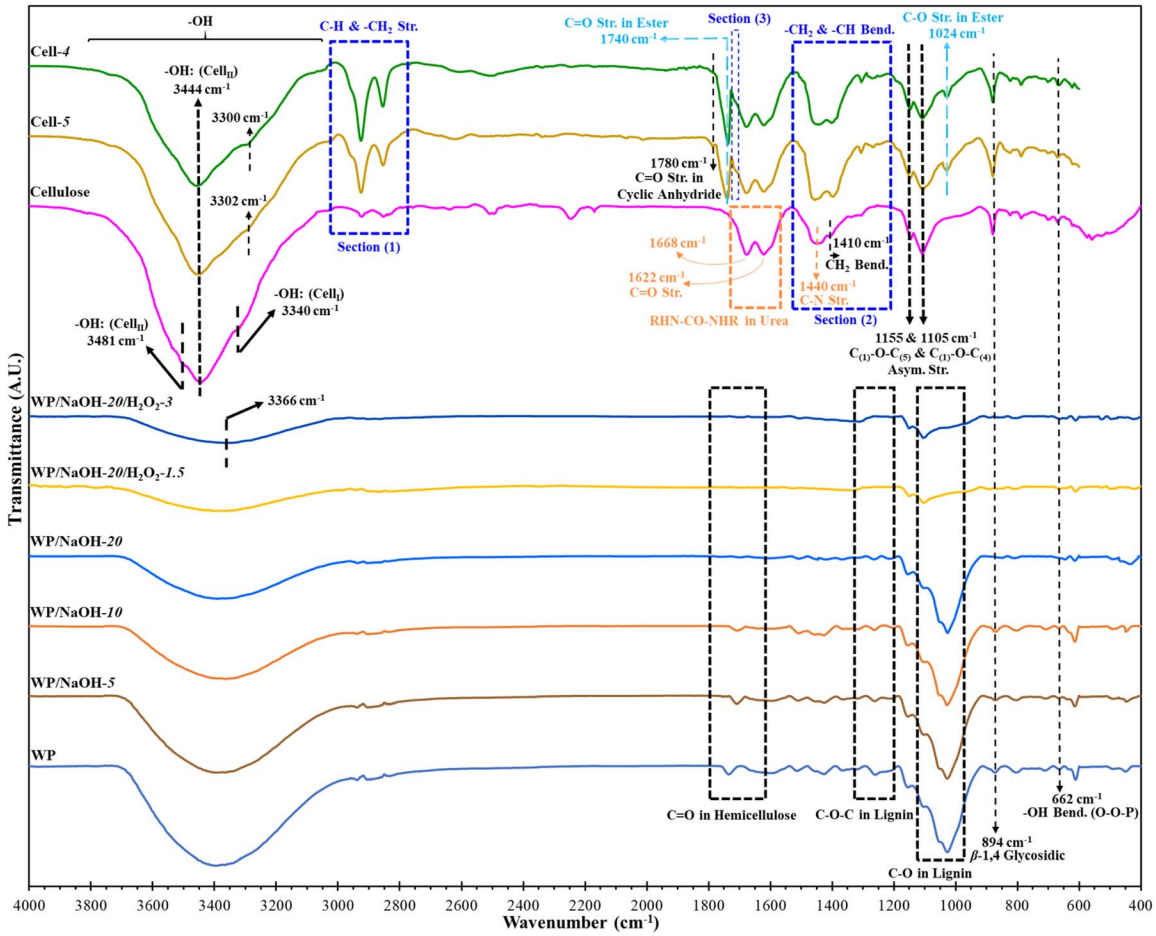

Fig. 3 FTIR-ATR spectrum of WP, (WP/NaOH-*x*), (WP/NaOH-*x*/H_2O_2-*y*), extracted cellulose powder from WP and (cell-5) and (cell-4) hydrogels.

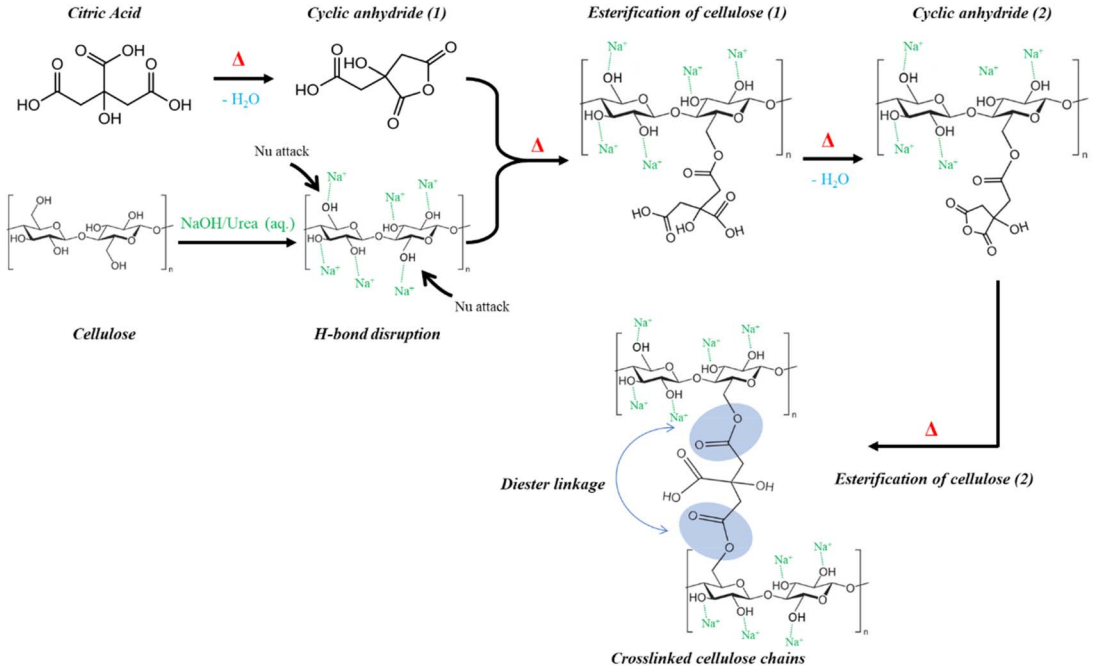

Fig. 4 The cross-linking mechanism for (cell-5) and (cell-4) hydrogels by presence of CA in NaOH/urea (aq.) medium.[13]

the 1020–1600 cm^{-1} region. This disappearance suggests significant removal of lignin from the samples. Additionally, the small peaks around 1300–1375 cm^{-1}, related to S=O and N–H bonds from ink compounds,[30] are absent after bleaching, indicating removal of both lignin and ink. Since (WP/NaOH-20/H_2O_2-1.5) and (WP/NaOH-20/H_2O_2-3) showed similar chemical characteristic results, the lower concentration sample (WP/NaOH-20/H_2O_2-1.5) was selected for cellulose extraction.

In the FTIR spectrum of extracted cellulose powder, polymorphs of cellulose are identified by the stretching vibration peaks of the –OH bond in the wavenumber of 3200–3600 cm^{-1} region. The peak at the wavenumber of 3340 cm^{-1} corresponds to –OH bonds of cellulose I ($cell_I$), while the peaks at the wavenumbers of 3444 cm^{-1} and 3481 cm^{-1} are attributed to hydrogen bonds in cellulose II ($cell_{II}$).[31] Dissolution in NaOH/urea solution at low temperatures can partially convert cellulose I to cellulose II[33,34] by breaking intermolecular hydrogen bonds and increasing cellulose swelling.[35,36] Peaks in the wavenumber of 800–1200 cm^{-1} range relate to C–O–C and β-glycosidic bonds in cellulose. Changes in peak intensity suggest partial conversion from cellulose I to cellulose II.[24,34] The yield of cellulose extraction was 16.52% of the initial WP grammage, with a cellulose purity of 78.3% according to the mass of the extracted cellulose powder before and after filtration with distilled water. Fig. 3 shows the FTIR spectra of (cell-5) and (cell-4) cellulose-based hydrogels, along with the interaction between citric acid (CA) as the cross-linking agent and extracted cellulose from WP. The broad peak in the region of 3300–3500 cm^{-1} is attributed to the stretching vibration of the –OH group in cellulose I and II, confirming the presence of hydroxyl groups in (cellulose) as well as in (cell-5) and (cell-4) hydrogels.[37] As the pH decreases, the peak at the wavenumber of 3340 cm^{-1} shifts to 3300 cm^{-1} for (cell-4). The decreased intensity of the –OH peak, compared to non-cross-linked (cellulose), confirms the chemical interaction between hydroxyl and carboxyl groups during cross-linking with CA, leading to fewer hydrogen bonds due to esterification.[26,38,39] The increased intensity of the peak at the wavenumber of 894 cm^{-1}, relating to the stretching vibration of the β-1,4 glycosidic bond in hydrogels, indicates decreased crystallinity during hydrogel formation. Section 1 of Fig. 3 shows peaks related to the stretching vibrations of $–CH_2$ and aliphatic C–H groups at the wavenumbers of 2933 cm^{-1} and 2868 cm^{-1}, respectively, characteristic of carbohydrates like cellulose, confirmed by a strong ether group peak.[37,40] Section 2 shows a peak for the bending vibration of $–CH_2$ at the wavenumber of 1410 cm^{-1}, stronger in cross-linked hydrogels.[24] Peaks at the wavenumbers of 1668 cm^{-1} and 1622 cm^{-1} confirm the presence of urea components in (cell-5) and (cell-4).[33] A new peak at the wavenumber of 1740 cm^{-1}, observed only in cross-linked hydrogels, is associated with the carbonyl group (C=O) of the ester bond formed after adding CA, indicating an esterification reaction between hydroxyl groups in cellulose and carboxyl groups in CA.[39,41,42] Peaks at the wavenumbers of 1024 cm^{-1} and 1273 cm^{-1}, related to C–O stretching in the ester group, were present only in cross-linked hydrogels, confirming successful cellulose cross-linking and hydrogel synthesis.[38] Section 3 shows a C=O stretching vibration at wavenumber of 1699 cm^{-1}, suggesting the carbonyl bond of the carboxyl group in CA.[11] The process involves the addition of NaOH/urea (aq.) solution, which changes the physical and chemical structure of cellulose by disrupting hydrogen bonds and hydrophobic interactions, crucial for hydrogel formation.[25,33] Initially, urea disrupts the hydrogen bonds of cellulose, making active sites vulnerable to nucleophilic attacks, targeting points for cross-

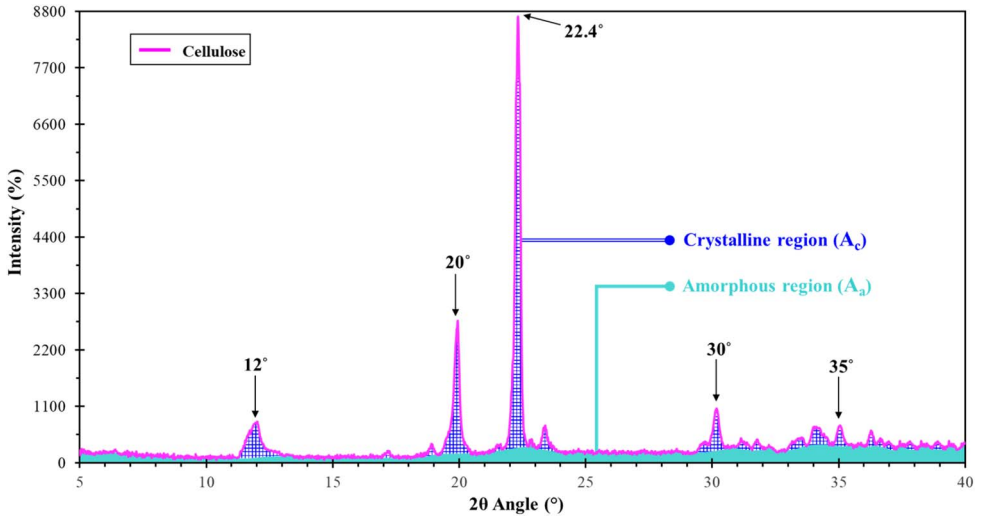

Fig. 5 XRD pattern of extracted cellulose powder from WP.

linking agents. Subsequently, nucleophilic–electrophilic interactions occur after adding NaOH/urea (aq.) solution, leading to chemical cross-linking of cellulose and the formation of 3-dimensional hydrogel networks.[13,25] At high temperatures, citric acid (CA) bonds with cellulose's hydrophilic –OH groups through a double esterification mechanism involving an anhydride intermediate.[37,39] The cross-linking reaction with CA involves forming an intramolecular cyclic anhydride by dehydrating carboxylic acids in CA, followed by further dehydration to form other intramolecular anhydrides.[41] The esterification reaction between cyclic anhydrides and the hydroxyl groups of cellulose creates cross-linking between cellulose chains, forming the (cell-5) and (cell-4) hydrogel networks.[9] This esterification stage is slower due to steric hindrance from large macromolecules (cellulose chains).[24] The cross-linking mechanism between cellulose and CA is illustrated in Fig. 4.[13]

4.2. Crystallization measurements of extracted cellulose from WP

To gain a better insight into the crystalline structure of the extracted cellulose from WP, XRD test was carried out on the extracted cellulose powder and the results are shown in Fig. 5. The peaks related to the structure of cellulose I and II can be seen at the 2θ angles of 12°, 20°, 22.4° and 35°.[31,38,43] This demonstrates that during the dissolution of cellulose in NaOH/urea (aq.) solution, cellulose Iβ is partially converted to cellulose II and its crystal structure is partially formed, while the other cellulose allomorph is still dominant. These findings are consistent with the FTIR results (Fig. 3). Therefore, it can be concluded that cellulose I was present in the extracted cellulose powder from WP (cellulose) after modification of NaOH/urea (aq.) solution and due to the low efficiency of mercerization, only a part of it has been converted to cellulose II.[26,31,33]

Using eqn (1), % X_C was calculated as 42.24%. This indicates the predominance of the amorphous part of extracted cellulose (Table 7).

Table 7 XRD data of the extracted cellulose powder from WP

A_c	A_a	% X_C	$A_{c\text{-cell.I}}$	% $X_{C\text{-cell.I}}$	$A_{c\text{-cell.II}}$	% $X_{C\text{-cell.II}}$
6862.94	9384.57	42.24	3279.02	20.18	1065.11	6.55

4.3. Microstructure characterization

4.3.1. Swelling measurements of (cell-5) and (cell-4) hydrogels. Equilibrium swelling theory was used to investigate the network structure and quantitatively determine the cross-links density (ν_c) in prepared hydrogels. Fig. 6 shows the effect of swelling on the hydrogel network. Swelling analysis indicated that with an increase in the cross-linking agent (CA) and a decrease in pH from 5 to 4, the amount of swelling (m_w/m_1) and the mass of water penetrating the hydrogels (m_w) decreased. This suggests that the porous structure of hydrogels at a lower pH (*i.e.*, equivalent to 4) is more consistent, making water penetration more difficult. Additionally, comparing the (m_3/m_1) ratio for (cell-5) and (cell-4) hydrogels showed that the weight loss during the drying stage after swelling was due to water evaporation, with the hydrogels' weights before and after the swelling test being relatively similar. The M_c and ν_c values for hydrogels are reported in Table 8, and their variations with pH changes are presented in Fig. 7(A) and (B). As shown in Table 8, increasing the value of CA increases the number of active sites for cross-linking, decreasing the distance between them. Consequently, the molecular weight between these chain connections (M_c) decreased from 10.55 kg mol^{-1} for (cell-5) to 7.59 kg mol^{-1} for (cell-4), and the cross-link density (ν_c) increased from 47.41 mol m^{-3} for (cell-5) to 65.89 mol m^{-3} for (cell-4). Under equilibrium swelling conditions, the network inside the (cell-5) and (cell-4) samples rearrange to accommodate water molecules as much as possible.[44] According to equilibrium swelling theory, immersing the (cell-5) and (cell-4)

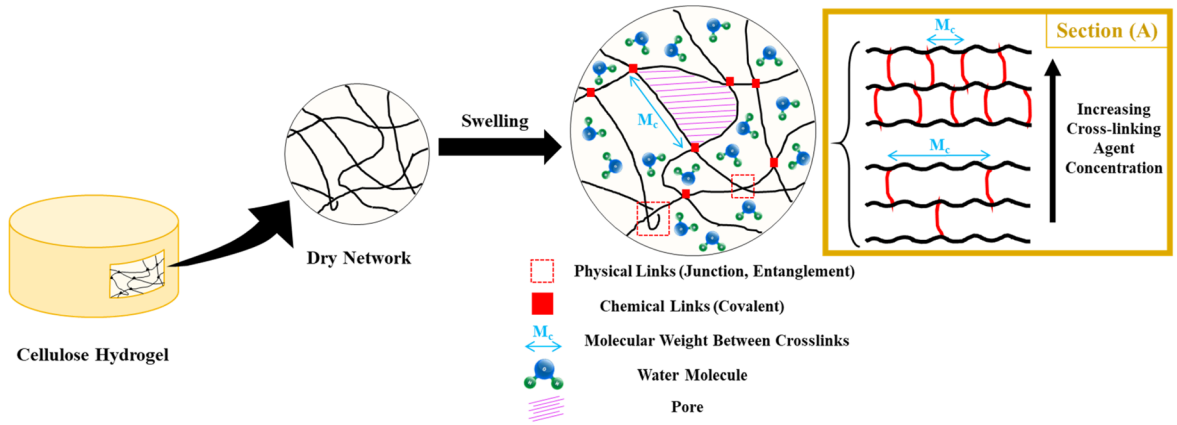

Fig. 6 Schematic of the effect of swelling and the amount of cross-linking agent on cellulose-based hydrogel network.

Table 8 Swelling parameters of (cell-5) and (cell-4) hydrogels networks

Sample	pH	m_3/m_1 (%)	m_w/m_1 (%)	ν_p	M_c (kg mol^{-1})	ν_c (mol m^{-3})
Cell-5	5	99.02 ± 0.53	363.13 ± 2.10	0.1204 ± 0.0006	10.55 ± 0.11	47.41 ± 0.54
Cell-4	4	98.59 ± 0.64	307.09 ± 2.29	0.1393 ± 0.0009	7.59 ± 0.11	65.89 ± 0.96

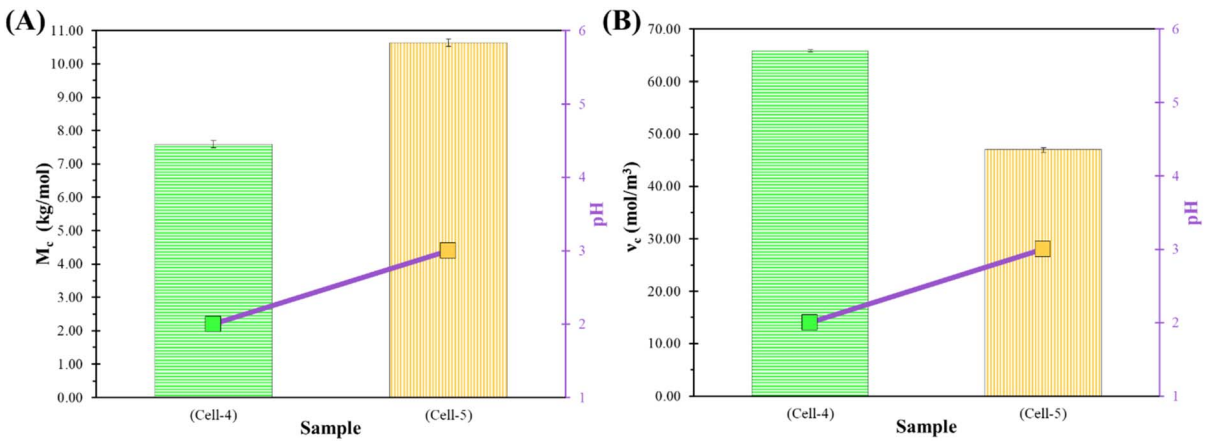

Fig. 7 Variation of: (A) M_c and (B) ν_c with pH alteration for (cell-5) and (cell-4) hydrogels.

samples in a solvent allows water molecules to penetrate the hydrogel chain. However, with increased cross-link density, there is less free space for water placement. According to Fig. 6 (section (A)), the (cell-4) sample with higher cross-link density likely has a lower water diffusion rate, leading to relatively lower swelling and decreased molecular weight between consecutive bonds.[22,45]

4.3.2. Density and porosity measurements. The apparent density, theoretical density, and percentage of porosity for, (cell-4), (cell-5) (cell-4/CF) and (cell-5/CF) and ultimately, (cell-4/CF/PEG) and (cell-5/CF/PEG) phase change composites (PCCs) are detailed in Table 9. (Cell-4) shows a higher porosity percentage due to the higher amount of CA used, which affects the cross-link density. Cellulose-based hydrogels, including those without carbon fiber (CF), tend to shrink in response to environmental conditions like temperature.[46] In other words, (cell-5) and (cell-4) hydrogels without CFs are less shape-stable and shrink due to moisture release, which causes reformation of hydrogen bonds and alters the network structure.[47] It is evident, CFs improve mechanical properties and maintain structural integrity, preventing shrinkage during evaporation drying by suppressing pore shrinkage and aiding in solvent exchange.[48] When molten PEG 2000 was added to (cell-5) and (cell-4) hydrogels, the samples expanded and lacked shape stability. The addition of CFs, however, led to stable geometrical shapes even with the PEG 2000 PCM.[47] The presence of CFs in (cell-5/CF) and (cell-4/CF) hydrogels reduced porosity, and further

Table 9 Apparent and theoretical density and percentage of porosity data of hydrogels, hydrogel/CFs and hydrogel/PCCs

Sample	Apparent density (kg m^{-3})	Theoretical density (kg m^{-3})	Porosity (%)
Cell-5	103.40 ± 0.08	2030.83	94.90
Cell-4	167.06 ± 0.04	2030.83	91.77
Cell-5/CF	298.82 ± 0.09	2028.60	85.26
Cell-4/CF	510.87 ± 0.10	2028.93	74.82
Cell-5/CF/PEG	943.75 ± 0.09	1329.36	29.00
Cell-4/CF/PEG	1016.85 ± 0.09	1413.80	28.07

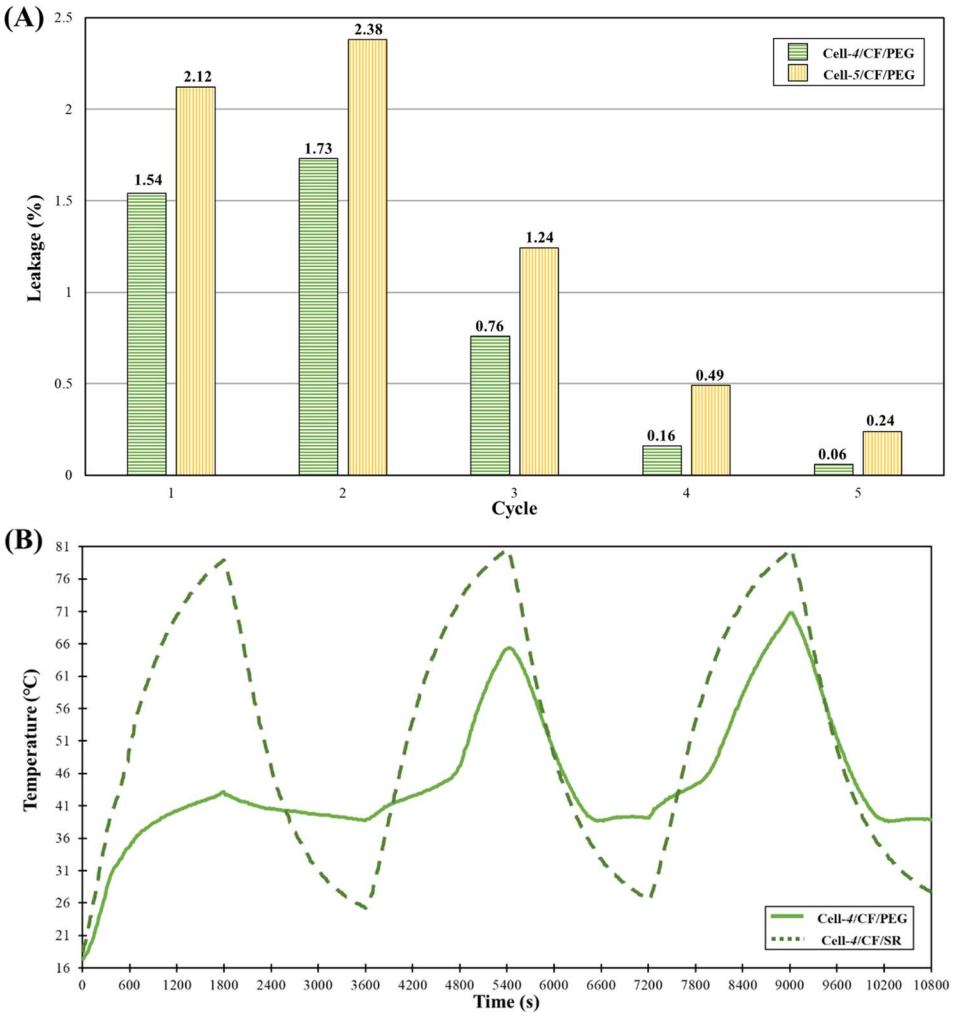

Fig. 8 (A) Leakage rate of (cell-4/CF/PEG) and (cell-5/CF/PEG) up to 5 consecutive cycles and (B) time–temperature history analysis curve of (cell-4/CF/PEG) and (cell-4/CF/SR) in 3 consecutive heating/cooling cycles (30 min/30 min).

reduction in porosity was observed in (cell-5/CF/PEG) and (cell-4/CF/PEG) PCCs as PEG 2000 filled most of the pores.

4.4. Leakage and thermal performance measurements

The structural stability of (cell-5/CF/PEG) and (cell-4/CF/PEG) phase change composites (PCCs) was evaluated through leakage tests over 5 heating and cooling cycles (see Fig. 2). As shown in Fig. 8(A), leakage rates decreased with each cycle, falling below 0.5% after the fourth cycle. After 5 cycles, the cumulative leakage rates were 4.25% for (cell-4/CF/PEG) and 6.47% for (cell-5/CF/PEG). Therefore, this sample was selected for further investigation.

Fig. 8(B) shows that during 3 consecutive heating/cooling cycles, (cell-4/CF/PEG) required more time to reach the desired temperature compared to the (cell-4/CF/SR) reference sample. This delay is attributed to the high latent heat of melting of PEG 2000 PCM. Despite this, compared to the

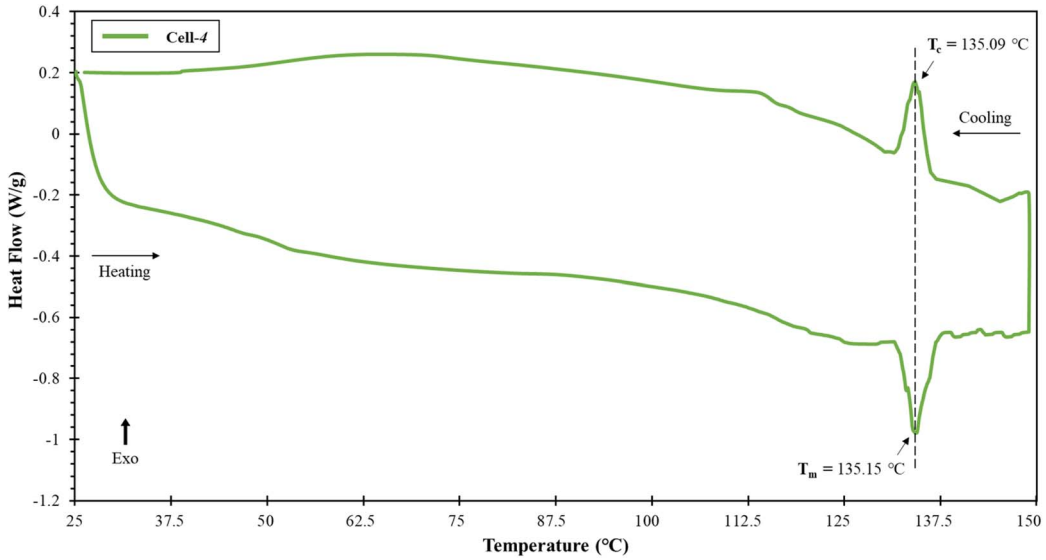

Fig. 9 DSC heating and cooling thermographs of dried (cell-4) hydrogel.

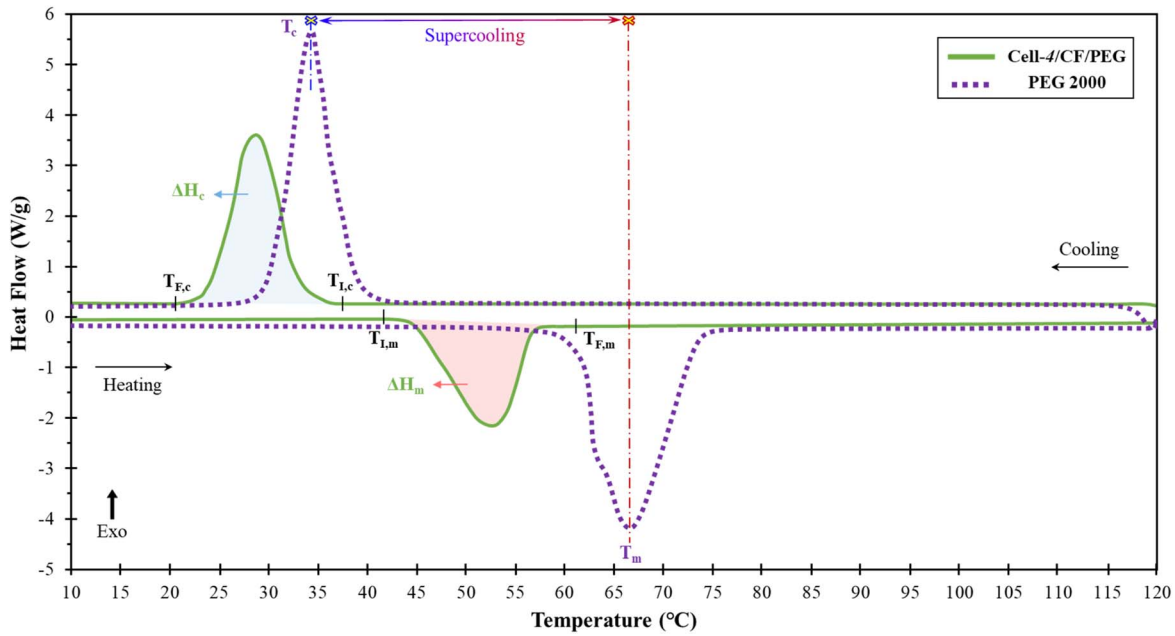

Fig. 10 DSC heating and cooling curves of (cell-4/CF/PEG) and pure PEG 2000.

reference sample, (cell-4/CF/PEG) demonstrated minimal leakage and stable shape during thermal phase transitions.

4.5. Thermal performance investigations

DSC curves were used to investigate the thermal properties of (cell-4), (cell-4/CF/PEG) phase change composite (PCC), and pure PEG 2000 PCM. Fig. 9 shows the DSC curve for the dried (cell-4) hydrogel. Since no peak was observed up to 130 °C, it indicates that the cross-linking reaction, which occurs at 80 °C, has been completed for (cell-4) hydrogel.[49] Furthermore, the peak observed in the temperature range of 132–136 °C, marked by an arrow on the curve, is likely related to the melting and crystallization of the remaining urea in the hydrogel.[50]

The DSC curves for (cell-4/CF/PEG) phase change composite (PCC) and pure PEG 2000 are shown in Fig. 10. Thermal properties including melting/crystallization temperatures, phase change enthalpies, melting enthalpy efficiencies, and supercooling degrees are listed in Table 10. As seen in Fig. 10, the melting peak of (cell-4/CF/PEG) is lower than that of pure PEG 2000. This decrease is attributed to the enhanced thermal conductivity (k) from CFs in the (cell-4/CF/PEG) composite, which improves heat transfer and creates a more uniform

Table 10 Thermal properties of (cell-4/CF/PEG) and pure PEG 2000

	Melting peak					Crystallization peak						
Sample	$T_{I,m}$[a] (°C)	T_m (°C)	$T_{F,m}$[b] (°C)	ΔH_m (J g^{-1})	ΔH_m (norm.) (J g^{-1})	$T_{I,c}$[a] (°C)	T_c (°C)	$T_{F,c}$[b] (°C)	ΔH_c (J g^{-1})	ΔH_c (norm.) (J g^{-1})	E (%)	T_{SC} (°C)
Cell-4/CF/PEG	40.41	51.28	61.31	104.87	163.32	35.67	27.45	20.28	87.28	135.92	89.81	23.83
PEG 2000	53.68	66.60	77.87	181.85	181.85	43.79	34.38	24.15	159.56	159.56	100.00	32.22

[a] $T_{I,m}$ and $T_{I,c}$ are the initial temperature of melting and crystallization peaks, respectively. [b] $T_{F,m}$ and $T_{F,c}$ are the final temperature of melting and crystallization peaks, respectively.

temperature distribution, leading to an earlier onset of melting compared to pure PEG 2000.

The supercooling degree is determined by the difference between the melting and crystallization temperatures of (cell-4/CF/PEG) and PEG 2000 PCM, as shown in eqn (7):[2,51]

$$T_{SC} = T_m - T_c \quad (7)$$

where T_{SC}, is the supercooling degree, and T_m and T_c are the melting and crystallizing temperatures, respectively. Supercooling, which drives PCMs to crystallize and release heat, is reduced in (cell-4/CF/PEG) due to potential nucleation sites provided by CFs, accelerating the crystallization process and altering the melting point compared to pure PEG 2000 PCM. The presence of CFs facilitates faster solidification and decreases T_{SC}.[51] A decrease in melting enthalpy (ΔH_m) and crystallinity, as observed in Fig. 10, is likely due to disruptions in PEG 2000's crystallization caused by the presence of CFs. ΔH_m, representing latent heat and energy storage capacity, is lower in (cell-4/CF/PEG) compared to pure PEG 2000. This drop is attributed to the reduced mass fraction of PEG 2000 in the composite. The theoretical enthalpy was calculated using eqn (8):[52]

$$\Delta H_T = x_{PEG} \times \Delta H_{PEG} \quad (8)$$

where x_{PEG} is the mass fraction of PEG 2000, which is 0.6421, leading to, ΔH_T. The addition of CFs affects crystallization by providing nucleation sites, allowing PEG 2000 chains to crystallize at lower temperatures, but also restricting chain mobility and disrupting the crystallization process. Melting enthalpy efficiency (E) was calculated using eqn (9):[52]

$$E = \frac{\Delta H_{m,sample}}{x_{PEG} \times \Delta H_{m,PEG}} \times 100 \quad (9)$$

Therefore, the calculated melting enthalpy efficiency of PEG 2000 in (cell-4/CF/PEG) is approximately 90%.

The thermal efficiency of the phase change composite (PCC) was evaluated through a time–temperature history analysis in a consecutive heating–cooling cycle. Fig. 11(A) shows the time–temperature history curve for (cell-4/CF/PEG) PCC. During heating, the temperature increased steadily until the 1100th second, reaching 45.5 °C after 1300 seconds. According to Fig. 11(B), the sample was initially in a two-phase (solid-molten) state as PEG 2000 PCM began to melt. After complete melting, the sample entered a single molten phase until the temperature reached around 77 °C (76.8 °C for (cell-4/CF/PEG)) at the 3020th second. The presence of CFs facilitated faster heat transfer, indicating improved thermal conductivity. During cooling, the temperature of (cell-4/CF/PEG) decreased rapidly with a slope of −0.261, reaching 37.9 °C after 1480 seconds. The cooling rate then slowed to −0.0020 and from the beginning of the cooling until 45 °C, the sample was in a single phase. After reaching 45 °C, the sample entered a two-phase (solid-molten) state during solidification. By the 10 050th second, the temperature had reached the ambient temperature (26.8 °C), and the PEG 2000 PCM had fully solidified. The CFs in the sample contributed to a continuous temperature reduction during solidification, preventing the temperature plot from plateauing.

According to Fig. 11(C), to investigate the performance of heat energy absorption and emission, the surface below the time–temperature history curves for (cell-4/CF/PEG) and (cell-4/CF/SR) systems were calculated according to eqn (10).

$$\text{Surface} : \frac{S_{control} - S_{sample}}{S_{control}} \times 100 \quad (10)$$

where $S_{control}$ and S_{sample}, are the area under the curve of (cell-4/CF/SR) and (cell-4/CF/PEG) phase change composite (PCC), respectively. To evaluate the amount of absorbed and emitted energy by the (cell-4/CF/PEG) phase change composite (PCC) in comparison with the (cell-4/CF/SR) reference sample, the area under the curve in the heating cycle (S_h), (up to 84 °C) and the area under the curve in the cooling cycle or S_c (up to 24 °C) were respectively obtained and reported in Table 11.

According to Table 11, (cell-4/CF/PEG) phase change composite (PCC) exhibited lower S_h values and higher S_c values compared to the (cell-4/CF/SR) reference sample. This suggests that the temperature increase in the 23–85 °C range started earlier for (cell-4/CF/SR). As shown in Fig. 11(C), it took 640 seconds for (cell-4/CF/SR) to reach 45.5 °C, whereas (cell-4/CF/PEG) reached this temperature after 1300 seconds, indicating a delay of 660 seconds. Additionally, the cooling rate was sharper for (cell-4/CF/SR) (−0.0377) compared to (cell-4/CF/PEG) (−0.0261). After 1480 seconds of cooling from 85 to 23 °C, (cell-4/CF/SR) reached 26.1 °C, while (cell-4/CF/PEG) was at 37.9 °C, reflecting the heat absorption and phase change behavior of PEG 2000 and the energy absorption/emission ratio indicates that (cell-4/CF/PEG) has about 70% stability.

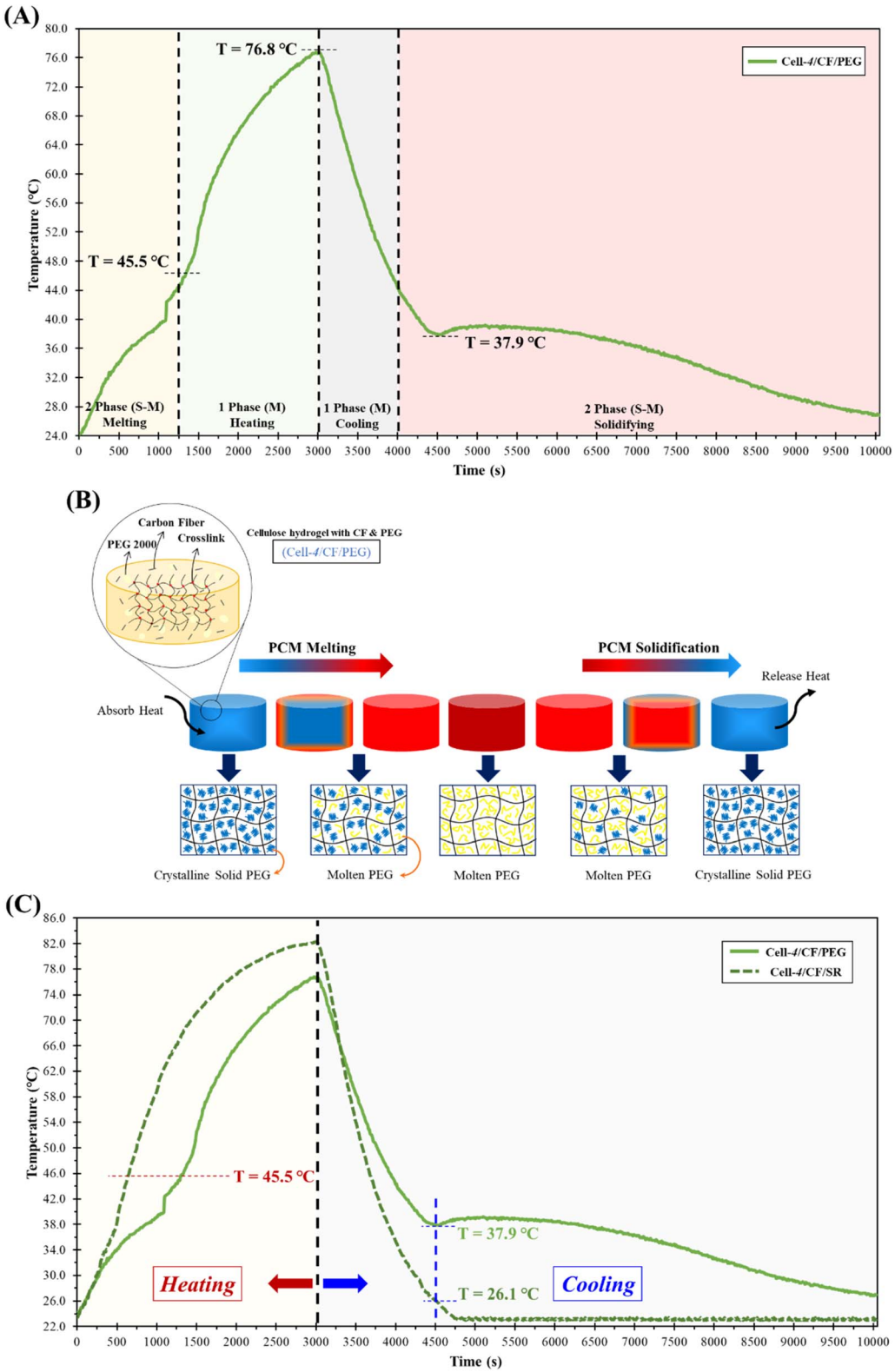

Fig. 11 (A) Time–temperature history curve of (cell-4/CF/PEG), (B) melting and solidification mechanism of PEG 2000 in (cell-4/CF/PEG) phase change composite (PCC) and (C) comparison between time–temperature history curve of (cell-4/CF/PEG) phase change composite (PCC) and (cell-4/CF/SR) reference sample.

Table 11 Time–temperature history curve parameters of (cell-4/CF/PEG) and (cell-4/CF/SR)

Sample	S_h (°C s)	ΔS_h	Energy absorption (%)	S_c (°C s)	ΔS_c	Energy emission (%)	Heating–cooling comparison (%)
Cell-4/CF/PEG	159 313.25	32 932.75	17.13	248 539.50	48 730.00	24.51	64.09
Cell-4/CF/SR	192 246.00	—	—	198 809.50	—	—	—

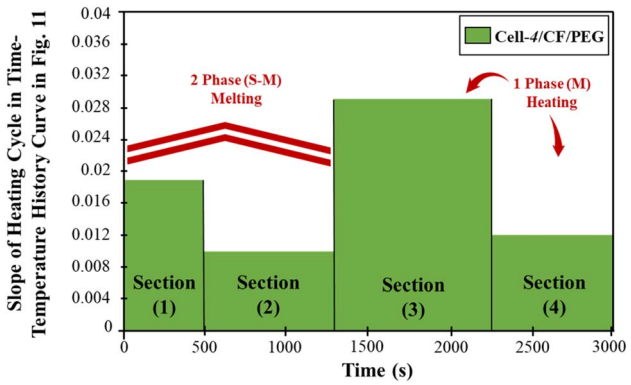

Fig. 12 Thermal diffusivity (α) index of (cell-4/CF/PEG).

The slope of the temperature–time history curve in the heating cycle, shown in Fig. 11(C), indicates thermal diffusivity (α). Lower thermal diffusivity suggests better thermal energy storage capability.[53] Fig. 12 illustrates the slope variation for (cell-4/CF/PEG). In section (1), during the heating cycle start, the temperature increase shows two-phase (solid-molten) behavior as PEG 2000 begins to melt. In section (2), during the phase change of PEG 2000, the lowest slope and thermal diffusivity are observed. Sections (3) and (4) show higher slopes due to the temperature exceeding 45.5 °C and complete melting of PEG 2000 PCM.

As illustrated in Fig. 13, thermal diffusivity (α) has been calculated for one-dimensional conditions of (cell-4/CF/PEG). Heat transfer equation as well as initial and boundary conditions (I.C. and B.C.) are presented in eqn (11) and (12), respectively.[51]

$$\frac{\partial T}{\partial t} = \alpha \frac{\partial^2 T}{\partial z^2} \tag{11}$$

$$\begin{cases} \text{I.C.} : @(t=0) \rightarrow T(z,0) = 25\ ^\circ\text{C} \\ \text{B.C.}_{\#1} : @(z=0) \rightarrow T(0,t) = 80\ ^\circ\text{C} \\ \text{B.C.}_{\#2} : @(z=h) \rightarrow T(h,t) = f(T,t) \end{cases} \tag{12}$$

Both curves in Fig. 14 indicated that, until the temperature of the center of the (cell-4/CF/PEG) phase change composite (PCC) reaches the melting point of PEG 2000 PCM, thermal diffusivity (α) stayed very low due to the presence of a solid phase and a molten phase (two-phase), as the PEG 2000 PCM in (cell-4/CF/PEG) phase change composite (PCC) is in melting process. Moreover, a solid phase remains until all the PCM present in the (cell-4/CF/PEG) phase change composite (PCC) has completely melted. Subsequently, with the increase in temperature of the (cell-4/CF/PEG) sample from around 45 °C and after all the PEG 2000 as the PCM melted, the thermal diffusivity (α) also increased.[54] The final thermal diffusivity (α) value of (cell-4/CF/PEG) phase change composite (PCC) was calculated as 8.2×10^{-9} m^2 s^{-1}.

Specific heat capacity (C_p) of (cell-4/CF/PEG) phase change composite (PCC) is calculated using the thermal energy balance

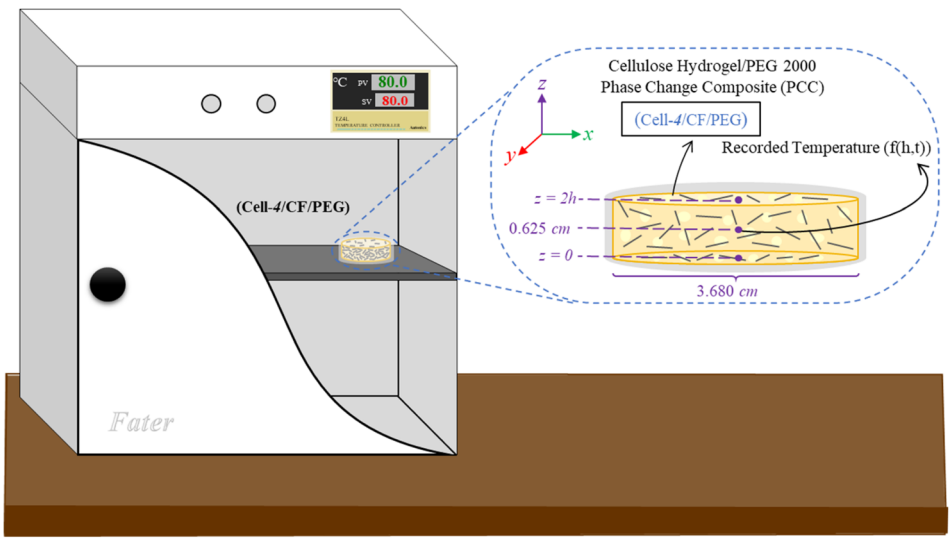

Fig. 13 Time–temperature history analysis set-up and the boundary conditions for thermal diffusivity (α) determination.

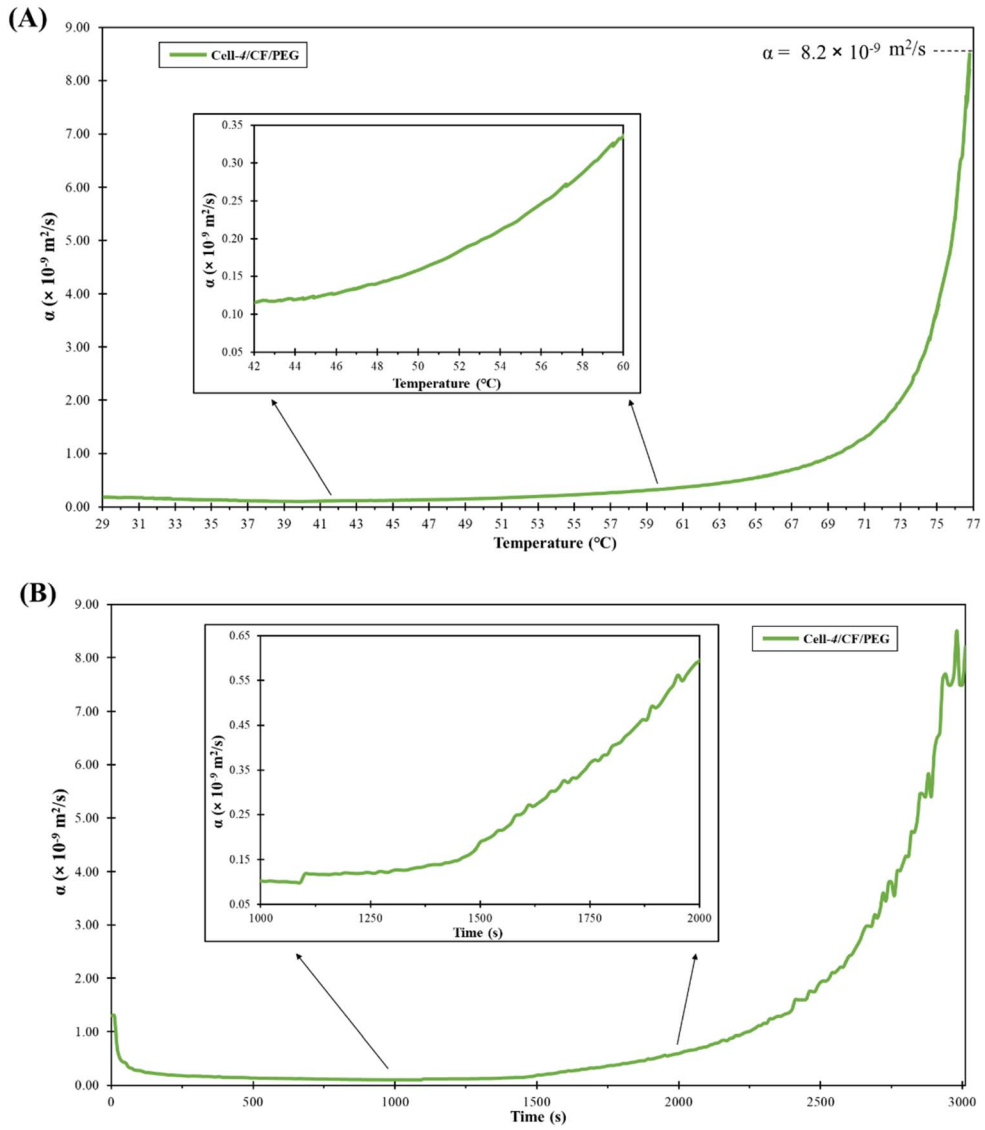

Fig. 14 Thermal diffusivity (α) values of (cell-4/CF/PEG) with alteration in: (A) temperature and (B) time.

represented by eqn (13) and (14), and considering the initial and boundary conditions in eqn (15) and (16) (Fig. 15).[55]

$$\rho C_{\mathrm{p}} \frac{\partial T}{\partial t} = K \frac{\partial^2 T}{\partial z^2} + Q_{\mathrm{crystal}} - hA\Delta T \tag{13}$$

$$Q_{\mathrm{crystal}} = \Delta H_{\mathrm{c}} \times \rho \times v_{\mathrm{crystal}} \tag{14}$$

$$\begin{cases} \mathrm{I.C.}: @(t=0) \rightarrow T(0,z) = T_{\mathrm{H}} \\ \mathrm{B.C._{\#1}}: @(z=0) \rightarrow \dfrac{\partial T}{\partial z} = 0 \\ \mathrm{B.C._{\#2}}: @\left(z = \dfrac{H}{2}\right) \rightarrow K\dfrac{\partial T}{\partial z} = h\left(\pi r^2\right)\Delta T \end{cases} \tag{15}$$

$$T(x,t) = T_{\infty} + (T_{\mathrm{i}} - T_{\infty})\exp\left(-\frac{hA}{\rho V C_{\mathrm{p}}}(t - t_0)\right) \tag{16}$$

where, T_{∞}, T_{i}, ρ, C_{p}, t_0 and t represent the ambient temperature, the temperature at the beginning of the cooling cycle, the density of the (cell-4/CF/PEG) phase change composite (PCC), the specific heat capacity, the starting time of the cooling cycle and the times after that, respectively. Moreover, v_{crystal} is the speed of the boundary movement of the interphase between solid-molten phases. The h parameter signifies the convective heat transfer coefficient of air, which is in the range of 2.5–25 W

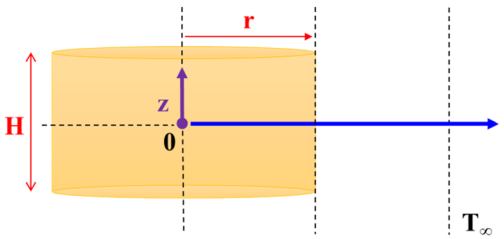

Fig. 15 The boundary conditions schematic of (cell-4/CF/PEG) sample for C_{p} determination.

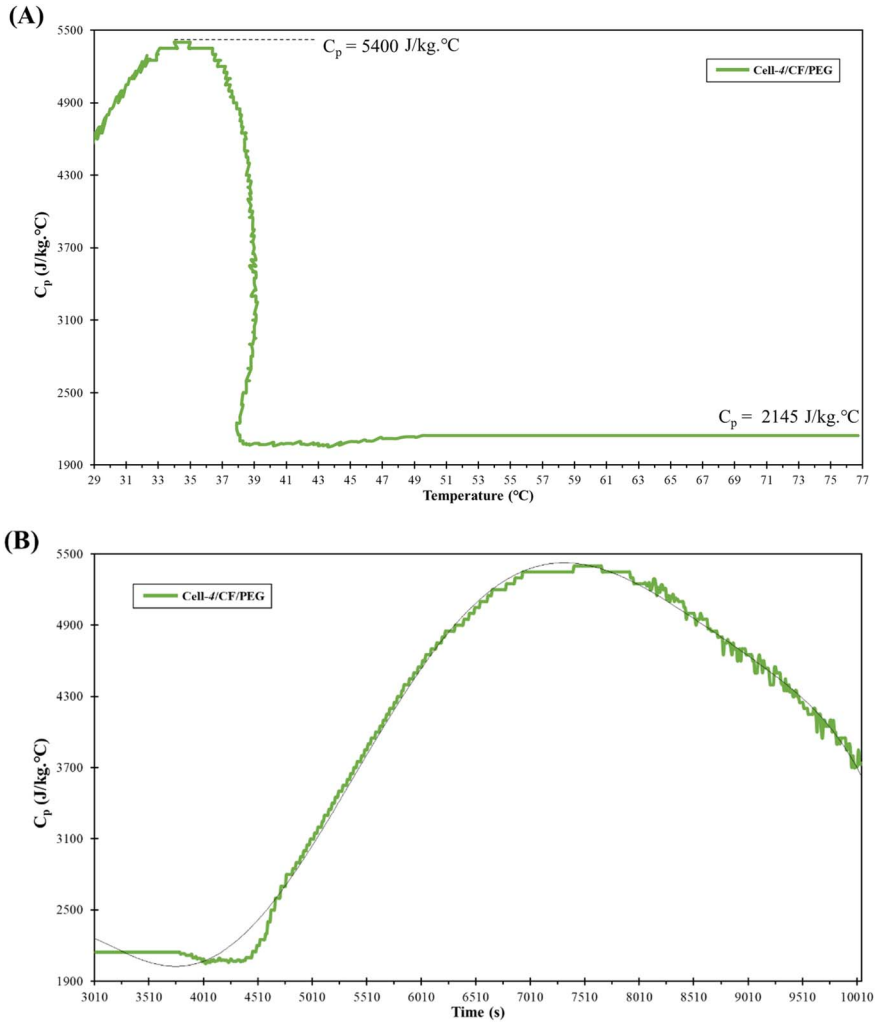

Fig. 16 Specific heat capacity (C_p) values of (cell-4/CF/PEG) with alteration in: (A) temperature and (B) time.

m^{-2} °C^{-1} in free convection, but was considered 12 W m^{-2} °C^{-1} in this study.[56] Also, A and V parameters are the surface of (cell-4/CF/PEG) sample in contact with the airflow (heat transfer surface) and the volume of the sample, which are obtained from eqn (17) and (18), respectively.

$$A = 2(\pi r^2) + 2\pi rH \quad (17)$$

$$V = H(\pi r^2) \quad (18)$$

where, r and H are the radius and the height of the cylindrical sample, respectively. Calculated values of C_p for (cell-4/CF/PEG) phase change composite (PCC) sample, are presented in Fig. 16. In the initial 770 s of the cooling cycle, when the sample had completely melted (at the highest temperature, *i.e.*, 76.8 °C), the C_p value for (cell-4/CF/PEG) is 2145 J kg^{-1} °C^{-1}. However, with the beginning of solidification which means that the temperature of all the PEG 2000 PCM has reached the melting point of PEG 2000 (where two-phase is solid-molten: solidifying), a significant rise in C_p values could be observed that reached 5400 J kg^{-1} °C^{-1}. This showed an escalation of approximately 151% in the specific heat capacity (C_p) for the (cell-4/CF/PEG) phase change composite (PCC). Additionally, C_p slightly decreased when going towards full solidification. With an increase in the specific heat capacity (C_p), thermal energy storage (TES) capacity improves and this reduces interior temperature fluctuations due to latent heat absorption.[53,57] Therefore, the fabricated (cell-4/CF/PEG) phase change composite (PCC) could perform well in terms of thermal energy storage applications and controlling thermal processes.

To investigate the effect of CFs along with the PCM (PEG 2000) on thermal conductivity (k) of the prepared phase change composite (PCC), effective thermal conductivity (k_{eff}) was calculated for (cell-4/CF/PEG) according to eqn (19).

$$k_{eff} = \alpha\rho C_p \quad (19)$$

where, ρ, C_p, and α represent the density, specific heat capacity (C_p), and thermal diffusivity (α) of the (cell-4/CF/PEG) phase change composite (PCC) sample. The variation of effective thermal conductivity (k_{eff}) values with changes in temperature for (cell-4/CF/PEG) is plotted in Fig. 17. According to Fig. 17, the

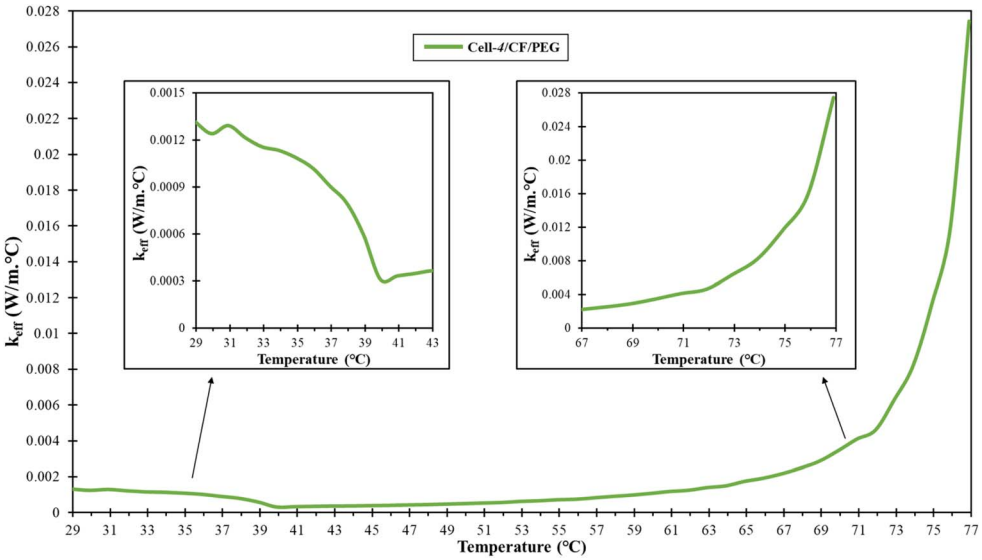

Fig. 17 Effective thermal conductivity coefficient (k_{eff}) values of (cell-4/CF/PEG) with temperature alteration.

Table 12 Comparison of thermal properties between the prepared cell-4/CF/PEG SS-PCM and similar SS-PCMs

SS-PCM	T_m[a] (°C)	ΔH_m (J g^{-1})	T_c[a] (°C)	ΔH_c (J g^{-1})	T_{SC} (°C)	k (W m^{-1} °C^{-1})	Leakage[b]	Reference
60 wt% paraffin + 40 wt% cellulose nanofibrils (CNFs)	55.4	173.6	48.1	171.9	7.3	0.037	Low	60
80 wt% paraffin + 20 wt% cellulose foam	49.0	148.5	54.7	150.4	5.7	0.077	Low	61
89.2 wt% PEG 6000 + 5.5 wt% cellulose aerogel + 5.3 wt% graphene nanoplatelets (GNPs)	63.0	156.1	44.3	148.9	18.7	1.60	Low	20
96.97 wt% PEG 6000 + 1.52 wt% microcrystalline cellulose (MCC) aerogel + 1.51 wt% graphene nanoplatelets (GNPs)	61.1	182.6	37.0	177.7	24.1	1.03	Low	62
50 wt% PEG 6000 + 25 wt% cellulose nanocrystalline (CNC) + 25 wt% reduced graphene oxide (rGO)	64.9	183.2	35.0	165.9	29.9	0.44	Low	63
80.1 wt% PEG 4000 + 19.9 wt% expanded graphite aerogel (EGA)	53.4	148.9	36.6	128.5	16.8	3.74	Low	64
95.3 wt% PEG 2000 + 2.87 wt% Fe_3O_4 + 1.83 wt% cellulose hydrogel	56.7	172.6	28.8	163.7	27.9	0.41	Low	65
64.21 wt% PEG 2000 + 0.75 wt% CF + 1.79 wt% cell-4	51.28	163.32	27.45	135.92	23.83	0.027	Low	Present work

[a] These values refer to the peak temperatures. [b] Leakage range: <5% = low, 5% ≪ 10% = medium, >10% = high.

trend of effective thermal conductivity (k_{eff}) is almost similar to that of thermal diffusivity (α) and reaches to 0.027 W m^{-1} °C^{-1}, when the entire PEG 2000 PCM had melted.[58] The effective thermal conductivity (k_{eff}) value was as low as 3.1 × 10^{-4} W m^{-1} °C^{-1}, when the system was two-phase as a consequence of the presence of a molten phase as well as a solid phase which is still reaching the melting temperature of PEG 2000 PCM. A slight increase in effective thermal conductivity (k_{eff}) value could be observed upon becoming single-phased, that is where all the PEG 2000 PCM in (cell-4/CF/PEG) phase change composite (PCC) has completely solidified.[59]

Table 12 compares the thermal properties of the SS-PCM in this study with those reported in other works. SS-PCMs with PW as the PCM generally exhibit lower supercooling temperatures (T_{SC}),[60,61] whereas those with PEG (varying molecular weights) tend to have T_{SC} values above 17 °C, reaching nearly 30 °C in some studies.[20,60,62–65] The thermal conductivity (k) of the SS-PCM in this study is quite lower than findings of ref. 20, 62 and 64 in the range of ~1–4 W m^{-1} °C^{-1}, lower than studies in ref. 63 and 65 with k being around 0.4 W m^{-1} °C^{-1}, and similar to findings of ref. 60 and 61. This indicates its suitability for both thermal insulation and energy storage applications.

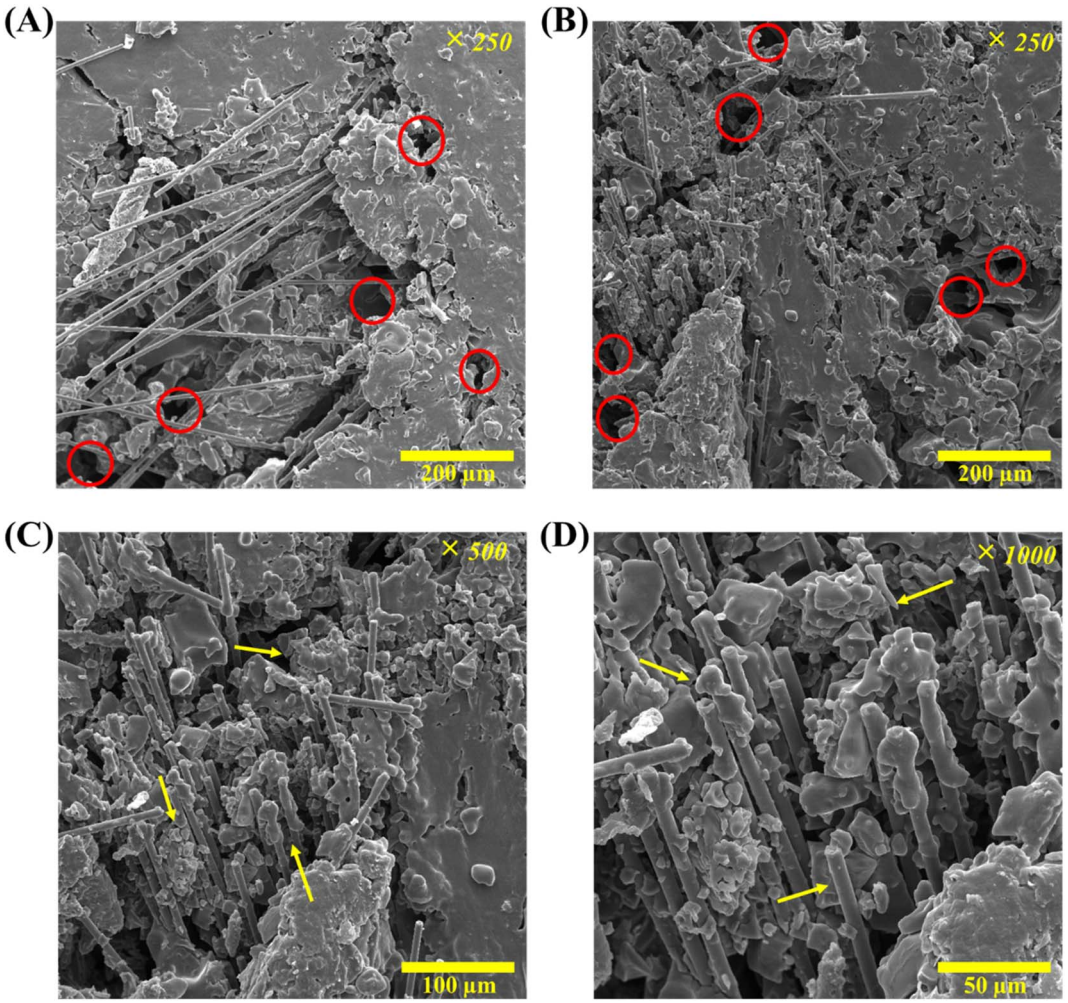

Fig. 18 FESEM micrographs of (cell-4/CF/PEG) in: (A) and (B) ×250 magnification and 200 μm scale, (C) ×500 magnification and 100 μm scale and (D) ×1000 magnification and 50 μm scale.

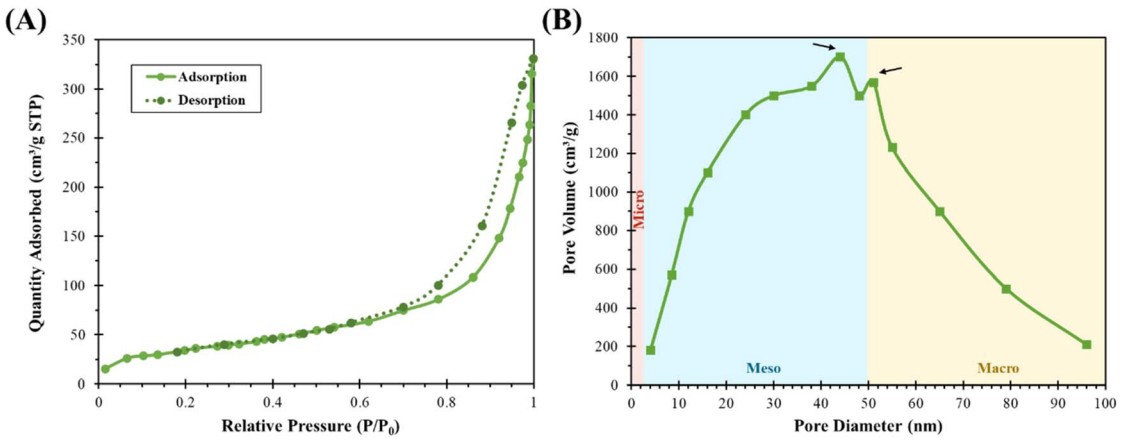

Fig. 19 (A) Nitrogen adsorption–desorption isotherm curve and (B) pore size distribution curve of (cell-4).

Additionally, based on leakage images and rates from this and other studies, all SS-PCMs maintain their shape stability with minimal liquid leakage.

4.6. Morphology characterization of (cell-4/CF/PEG) phase change composite (PCC)

The FESEM images of (cell-4/CF/PEG) are presented in Fig. 18. Macro pores related to the hydrogel structure (marked red

Table 13 BET specific surface parameter and BJH structural data of (cell-4)

S_{BET} ($m^2\ g^{-1}$)	S_{BET} single point[a] ($m^2\ g^{-1}$)	Cumulative V_{BJH} (ads.) ($cm^3\ g^{-1}$)	Cumulative V_{BJH} (des.) ($cm^3\ g^{-1}$)	Mesopores (%)	Average BJH pore diameter (ads.) (nm)	Average BJH pore diameter (des.) (nm)
216.51	199.23	0.42	0.39	80.35	50.09	45.09

[a] S_{BET} single point refers to BET specific surface at relative pressure (P/P_0) equal to 0.29.

circles) were distinguished in Fig. 18(A) and (B). Also, in Fig. 18 ((C) and (D)-marked arrows), CFs and PEG 2000 were observed on a micrometer scale. According to these images, it can be concluded that the structure of (cell-4/CF/PEG) is well oriented with a uniform distribution of PEG 2000 PCM all over the microstructure of the sample. Since the results of the thermal performance analysis were acceptable, this validated the findings of earlier tests and is in line with the research expectations.

Additionally, BET analysis was done in parallel with FESEM of (cell-4/CF/PEG) PCC to confirm the porous nanostructure of the selected (cell-4) hydrogel. Fig. 19(A) shows the nitrogen adsorption–desorption isotherms for the (cell-4) hydrogel. According to IUPAC classification, the isotherms for this sample correspond to type IV, with a type H1 hysteresis loop. The desorption curve is nearly parallel to the adsorption curve, indicating adsorption in materials with mesopores. The initial part of the isotherm at a relative pressure (P/P_0) below 0.05 corresponds to monolayer adsorption without restrictions, while the increase in physisorption volume in this region suggests the presence of micropores. Additionally, the nearly linear section of the isotherm ($P/P_0 > 0.05$) is typically associated with multilayer adsorption. The hysteresis loop, formed by the desorption isotherm, is commonly used to determine the shape of the porous structure, as it reflects capillary condensation in mesoporous materials at high P/P_0. This loop suggests the presence of open, cylindrical pores.[25]

Morphological properties of the pores, including specific surface area (S_{BET}), cumulative volume (V_{BJH}), mesopore percentage, and pore diameter of (cell-4), are listed in Table 13. Fig. 19(B) presents the pore size distribution of the (cell-4) hydrogel, revealing a mesoporous network with pore diameters ranging from 2 to 50 nm. This suggests that the hydrogel exhibits a nanostructured morphology.[24,66] Based on porosimetry data, the total pore volume and micropore volume are 0.56 $cm^3\ g^{-1}$ and 0.11 $cm^3\ g^{-1}$, respectively. The BET-specific surface area of the (cell-4) hydrogel in this study is 216.51 $m^2\ g^{-1}$, which is higher than the values reported by Hu *et al.*[24] (80–125 $m^2\ g^{-1}$) and Seantier *et al.*[66] (143–162 $m^2\ g^{-1}$) but relatively close to that reported by Kaya[67] (275 $m^2\ g^{-1}$).

5. Current market and cost benefits

Today, paper is a widely used material to make newspapers, books and magazines, Due to its wide use, the increase in production results an increase in waste and involves waste disposal problems. Cellulose can be obtained from commercial suppliers or extracted from waste materials, with recycled paper products like WP being one of the most economical and sustainable sources. Additionally, the recyclability of used WP presents a promising opportunity to replace the excessive and costly use of new raw materials.[68] Cellulose extracted from WP is a sustainable option, but the process involves several steps and considerations. WP, typically sourced from recycling centers or municipal waste streams, must first undergo pre-treatment to remove contaminants like inks, adhesives, and coatings. This involves shredding, washing, and de-inking through mechanical or chemical methods. Next, chemical treatments are used to remove impurities such as lignin and hemicellulose. The process could also require energy for mechanical pulping, bleaching, and chemical treatment, as well as labor for machinery operation, chemical management, and process oversight. The extracted cellulose is then dried and processed into a usable form for applications in industries like paper, textiles, pharmaceuticals, and food.[69] The cost of commercial cellulose varies significantly depending on its source (*e.g.*, wood, cotton) and grade (*e.g.*, nano, micro, or standard cellulose). It is typically sold in forms like MCC or cellulose powder, with purity, particle size, and supplier influencing its availability. Unlike cellulose extracted from waste materials, commercial cellulose is pre-purified and available in various

Table 14 Comparison of WP and commercial extracted cellulose

Factor		WP cellulose	Commercial cellulose
Cost (USD ($) per ton)	Raw material	100–150	1500–3000[a]
	Chemicals & energy[a]	600–1000	N/A
	Labor and equipment	100–300	N/A
	Total estimated	800–1450	1500–3000
Purity		Moderate (requires further refining)	High (ready-to-use)
Environmental impact		Low (recycling waste material)	Higher (industrial production)
Scalability		Limited by waste availability	High (industrial supply chain)

[a] The pricing is obtained from various websites including Alibaba[75] and Sigma-Aldrich.[76]

grades, making it a convenient option for larger industries. However, prices are subject to fluctuations due to global supply and demand dynamics.[70]

The global newspaper publishing market is projected to grow from USD 88.05 billion in 2024 to USD 146.85 billion by 2034, at a 5.2% compound annual growth rate (CAGR), while the printing paper market, valued at USD 45.6 billion in 2024, is expected to reach USD 98.7 billion by 2033, growing at a 5.9% CAGR. Similarly, the pulp and paper industry, valued at USD 360 billion in 2024, is anticipated to expand to over USD 391 billion by 2032 at a 1% CAGR, reflecting steady growth across these interconnected sectors. Meanwhile, the global waste paper recycling market, valued at USD 45.60 billion in 2023, is forecasted to grow at a 4.8% CAGR, reaching USD 63.32 billion by 2030, driven by environmental awareness, government regulations, and increasing demand for sustainable packaging. The Asia-Pacific region dominates this market due to high demand in countries like India and China, while Europe is expected to grow at a faster CAGR of 6.9%, supported by strong recycling rates and raw material demand. Despite challenges such as rising raw material costs, wood pulp reached USD 1200 per metric ton in 2022, and competition from digital and plastic alternatives, advancements in recycling technologies and growing demand for paper-based packaging present significant growth opportunities.[71–74] Detailed information about the costs associated with extracting cellulose from WP and commercial cellulose is presented in the Table 14.

6. Conclusion

In this study, the suitability of the designed cross-linked network of cellulose-based hydrogel and the presence of CFs for the shape stability of the PEG 2000 PCM was investigated. The yield and purity of the cellulose extraction process from WP *via* an alkaline-peroxide treatment was calculated as about 17% and 78%, respectively. Chemical and microstructural studies have shown that the cross-linked hydrogels possess macro and meso pores for storing PEG 2000 PCM. By the incorporation of conductive fillers of CFs into the porous structure of cellulose-based hydrogel, geometrical stability was enhanced as no shrinkage was observed. Controlling the concentration of the cross-linking agent (CA), *i.e.*, pH values equivalent to 4 and 5, and CFs led to the adjustment of the swelling-leakage behavior along with the latent heat of melting. Thus, a shape stable phase change composite (PCC) was successfully fabricated through impregnation of molten PEG 2000 PCM into a cellulose-based hydrogel-CFs composite. Furthermore, the leakage rate of the prepared (cell-4/CF/PEG) phase change composite (PCC) including cellulose-based hydrogel, CFs and PEG 2000 PCM, reached out to 4.25 wt% after five heating–cooling cycles. Moreover, the (cell-4/CF/PEG) phase change composite (PCC) was synthesized with an enthalpy efficiency of 90% and an 80% increase of the effective thermal conductivity reaching 0.027 W m^{-1} $°C^{-1}$. The thermal energy storage (TES) capacity of the synthesized (cell-4/CF/PEG) phase change composite (PCC) was measured to be about 25% from theoretical methods and thermal energy absorption-emission models in successive heating/cooling cycles. Morphological studies confirmed the orientation of CFs as well as uniform distribution of PEG 2000 PCM all over the microstructure of (cell-4/CF/PEG) phase change composite (PCC), which could result in an acceptable and high thermal performance. The contrast between thermal conductivity, porosity, impregnation, and leakage is thought to determine a PCC's thermal performance, as it is important for optimizing to reach a higher efficiency of thermal energy storage.

Data availability

Data for this article, including DSCs and time temperature history calculations, FESEMs, FTIRs, XRDs, leakages and swellings and porosities, and nitrogen adsorption–desorption parameters, is available at Open Science Framework at **https://doi.org/10.17605/OSF.IO/TVYZW**.

Conflicts of interest

There are no confilicts to declare.

Acknowledgements

The authors would like to thank Tarbiat Modares University, Iran Nanotechnology Initiative Council (INIC) for supporting this research work.

References

1 A. Islam, A. K. Pandey, R. Saidur, B. Aljafari and V. V. Tyagi, Advancements in foam-based phase change materials: unveiling leakage control, enhanced thermal conductivity, and promising applications, *J. Energy Storage*, 2023, **74**, 109380.

2 Y. Jia, Y. Jiang, Y. Pan, X. Zou, Q. Zhang, X. Gao, J. Zhang, K. Yu, Y. Yang and Y. Liu, Recent advances in energy storage and applications of form-stable phase change materials with recyclable skeleton, *Carbon Neutralization*, 2024, **3**(2), 313–343.

3 Y. E. Milián, A. Gutiérrez, M. Grageda and S. Ushak, A review on encapsulation techniques for inorganic phase change materials and the influence on their thermophysical properties, *Renew. Sustain. Energy Rev.*, 2017, **73**, 983–999.

4 M. I. Khan, F. Asfand and S. G. Al-Ghamdi, Progress in research and development of phase change materials for thermal energy storage in concentrated solar power, *Appl. Therm. Eng.*, 2023, **219**, 119546.

5 Q. Al-Yasiri and M. Szabó, Incorporation of phase change materials into building envelope for thermal comfort and energy saving: a comprehensive analysis, *J. Build. Eng.*, 2021, **36**, 102122.

6 H. Gao, J. Wang, X. Chen, G. Wang, X. Huang, A. Li and W. Dong, Nanoconfinement effects on thermal properties of nanoporous shape-stabilized composite PCMs: a review, *Nano Energy*, 2018, **53**, 769–797.

7 H. R. Hasan and M. H. Sauodi, Novel method for extraction of cellulose from agricultural and industrial wastes, *Indian J. Chem. Technol.*, 2014, **9**(4), 148–153.
8 R. Kundu, P. Mahada, B. Chhirang and B. Das, Cellulose hydrogels: green and sustainable soft biomaterials, *Curr. Res. Green Sustainable Chem.*, 2022, **5**, 100252.
9 S. Bhaladhare and D. Das, Cellulose: a fascinating biopolymer for hydrogel synthesis, *J. Mater. Chem. B*, 2022, **10**(12), 1923–1945.
10 S. Zafar, M. Hanif, M. Azeem, K. Mahmood and S. A. Gondal, Role of crosslinkers for synthesizing biocompatible, biodegradable and mechanically strong hydrogels with desired release profile, *Polym. Bull.*, 2022, **79**(11), 9199–9219.
11 S. H. Zainal, R. Nofrianti, A. M. Lazim and R. Othaman, Cellulose-based hydrogel as Halal agricultural medium, *Malays. Appl. Biol.*, 2019, **48**(2), 109–113.
12 S. Widiarto, S. D. Yuwono, A. Rochliadi and I. M. Arcana, Preparation and characterization of cellulose and nanocellulose from agro-industrial waste-cassava peel, *IOP Conf. Ser.: Mater. Sci. Eng.*, 2017, **176**(1), 012052.
13 M. M. Golor, D. Rosma, S. P. Santoso, F. Soetaredjo, M. Yuliana, S. Ismadji and A. Ayucitra, Citric acid-crosslinked cellulosic hydrogel from sugarcane bagasse: preparation, characterization, and adsorption study, *J. Indones. Chem. Soc.*, 2020, **3**, 59–67.
14 H. Nasution, H. Harahap, N. F. Dalimunthe, M. H. Ginting, M. Jaafar, O. O. Tan, H. K. Aruan and A. L. Herfananda, Hydrogel and effects of crosslinking agent on cellulose-based hydrogels: a review, *Gels*, 2022, **8**(9), 568.
15 T. Khadiran, M. Z. Hussein, Z. Zainal and R. Rusli, Encapsulation techniques for organic phase change materials as thermal energy storage medium: a review, *Sol. Energy Mater. Sol. Cells*, 2015, **143**, 78–98.
16 N. Nazari, A. R. Bahramian and A. Allahbakhsh, Thermal storage achievement of paraffin wax phase change material systems with regard to Novolac aerogel/carbon monofilament/zinc borate form stabilization, *J. Energy Storage*, 2022, **50**, 104741.
17 Q. Al-Yasiri and M. Szabó, Paraffin as a phase change material to improve building performance: an overview of applications and thermal conductivity enhancement techniques, *Renewable Energy Environ. Sustainability*, 2021, **6**, 38.
18 L. Chen, R. Zou, W. Xia, Z. Liu, Y. Shang, J. Zhu, Y. Wang, J. Lin, D. Xia and A. Cao, Electro-and photodriven phase change composites based on wax-infiltrated carbon nanotube sponges, *ACS Nano*, 2012, **6**(12), 10884–10892.
19 K. Kant, P. H. Biwole, I. Shamseddine, G. Tlaiji, F. Pennec and F. Fardoun, Recent advances in thermophysical properties enhancement of phase change materials for thermal energy storage, *Sol. Energy Mater. Sol. Cells*, 2021, **231**, 111309.
20 J. Yang, E. Zhang, X. Li, Y. Zhang, J. Qu and Z. Z. Yu, Cellulose/graphene aerogel supported phase change composites with high thermal conductivity and good shape stability for thermal energy storage, *Carbon*, 2016, **98**, 50–57.
21 X. Fan, Y. Guan, Y. Li, H. Y. Yu, J. Marek, D. Wang, J. Militky, Z. Y. Zou and J. Yao, Shape-stabilized cellulose nanocrystal-based phase-change materials for energy storage, *ACS Appl. Nano Mater.*, 2020, **3**(2), 1741–1748.
22 D. Y. Kim, J. W. Park, D. Y. Lee and K. H. Seo, Correlation between the crosslink characteristics and mechanical properties of natural rubber compound via accelerators and reinforcement, *Polymers*, 2020, **12**(9), 2020.
23 Z. Xia, M. Patchan, J. Maranchi, J. Elisseeff and M. Trexler, Determination of crosslinking density of hydrogels prepared from microcrystalline cellulose, *J. Appl. Polym. Sci.*, 2013, **127**(6), 4537–4541.
24 Y. Hu, S. Li, T. Jackson, H. Moussa and N. Abidi, Preparation, Characterization, and Cationic Functionalization of Cellulose-Based Aerogels for Wastewater Clarification, *J. Mater.*, 2016, **2016**(1), 3186589.
25 M. M. Yashim, M. Mohammad, N. Asim and A. Fudholi, Structure and properties of monolithic cellulose aerogels prepared from oil palm cellulose microfiber (OPMFC) using alkaline/urea solvent system potentially for solar thermal applications, *J. Sol-Gel Sci. Technol.*, 2023, **108**(1), 47–59.
26 M. El-Sakhawy, S. Kamel, A. Salama and H. A. Tohamy, Preparation and infrared study of cellulose based amphiphilic materials, *Cellul. Chem. Technol.*, 2018, **52**(3–4), 193–200.
27 R. Javier-Astete, J. Jimenez-Davalos and G. Zolla, Determination of hemicellulose, cellulose, holocellulose and lignin content using FTIR in Calycophyllum spruceanum (Benth.) K. Schum. and Guazuma crinita Lam, *PLoS One*, 2021, **16**(10), e0256559.
28 W. H. Danial, Z. A. Majid, M. N. M. Muhid, M. B. Bakar, Z. Ramli and S. Triwahyono, Preparation of cellulose nanocrystal aerogel from wastepaper through freeze-drying technique, *Adv. Mater. Res.*, 2015, **1125**, 296–300.
29 S. Cheng, A. Huang, S. Wang and Q. Zhang, Effect of Different Heat Treatment Temperatures on the Chemical Composition and Structure of Chinese Fir Wood, *BioResources*, 2016, **11**(2), 4006–4016.
30 S. F. Hanafiah, W. H. Danial, M. A. Samah, W. Z. Samad, D. Susanti, R. M. Salim and Z. A. Majid, Extraction and characterization of microfibrillated and nanofibrillated cellulose from office paper waste, *Malays. J. Anal. Sci.*, 2019, **23**(5), 901–913.
31 K. Kafle, K. Greeson, C. Lee and S. H. Kim, Cellulose polymorphs and physical properties of cotton fabrics processed with commercial textile mills for mercerization and liquid ammonia treatments, *Text. Res. J.*, 2014, **84**(16), 1692–1699.
32 W. Farhat, R. Venditti, A. Quick, M. Taha, N. Mignard, F. Becquart and A. Ayoub, Hemicellulose extraction and characterization for applications in paper coatings and adhesives, *Ind. Crops Prod.*, 2017, **107**, 370–377.
33 M. A. Fauziyah, W. Widiyastuti, R. Balgis and H. Setyawan, Production of cellulose aerogels from coir fibers via an alkali–urea method for sorption applications, *Cellulose*, 2019, **26**, 9583–9598.

34 S. Zhang, F. Zhang, L. Jin, B. Liu, Y. Mao, Y. Liu and J. Huang, Preparation of spherical nanocellulose from waste paper by aqueous NaOH/thiourea, *Cellulose*, 2019, **26**, 5177–5185.

35 Z. Jiang, Y. Fang, J. Xiang, Y. Ma, A. Lu, H. Kang, Y. Huang, H. Guo, R. Liu and L. Zhang, Intermolecular interactions and 3D structure in cellulose–NaOH–urea aqueous system, *J. Phys. Chem. B*, 2014, **118**(34), 10250–10257.

36 H. Qi, C. Chang and L. Zhang, Effects of temperature and molecular weight on dissolution of cellulose in NaOH/urea aqueous solution, *Cellulose*, 2008, **15**, 779–787.

37 S. Durpekova, K. Filatova, J. Cisar, A. Ronzova, E. Kutalkova and V. Sedlarik, A novel hydrogel based on renewable materials for agricultural application, *Int. J. Polym. Sci.*, 2020, **2020**(1), 8363418.

38 Y. Kim, D. Jeong, K. H. Park, J. H. Yu and S. Jung, Efficient adsorption on benzoyl and stearoyl cellulose to remove phenanthrene and pyrene from aqueous solution, *Polymers*, 2018, **10**(9), 1042.

39 M. G. Raucci, M. A. Alvarez-Perez, C. Demitri, D. Giugliano, V. De Benedictis, A. Sannino and L. Ambrosio, Effect of citric acid crosslinking cellulose-based hydrogels on osteogenic differentiation, *J. Biomed. Mater. Res., Part A*, 2015, **103**(6), 2045–2056.

40 A. P. Almeida, J. N. Saraiva, G. Cavaco, R. P. Portela, C. R. Leal, R. G. Sobral and P. L. Almeida, Crosslinked bacterial cellulose hydrogels for biomedical applications, *Eur. Polym. J.*, 2022, **177**, 111438.

41 D. Das, P. Prakash, P. K. Rout and S. Bhaladhare, Synthesis and characterization of superabsorbent cellulose-based hydrogel for agriculture application, *Starch/Staerke*, 2021, **73**(1–2), 1900284.

42 D. L. Pavia, G. M. Lampman, G. S. Kriz and J. R. Vyvyan, *Introduction to Spectroscopy*, Cengage Learning, 2015.

43 S. Nam, A. D. French, B. D. Condon and M. Concha, Segal crystallinity index revisited by the simulation of X-ray diffraction patterns of cotton cellulose Iβ and cellulose II, *Carbohydr. Polym.*, 2016, **135**, 1–9.

44 F. T. Borges, G. Papavasiliou and F. Teymour, Characterizing the molecular architecture of hydrogels and crosslinked polymer networks beyond Flory–Rehner—I. Theory, *Biomacromolecules*, 2020, **21**(12), 5104–5118.

45 H. Omidian, S. A. Hasherni, F. Askari and S. Nafisi, Swelling and crosslink density measurements for hydrogels, *Iran. J. Polym. Sci. Technol.*, 1994, **3**(2), 115–119.

46 M. J. C. de Sá, G. G. de Lima, F. A. D. S. Segundo and M. J. D. Nugent, Structure response for cellulose-based hydrogels via characterization techniques, in *Cellulose-Based Superabsorbent Hydrogels. Polymers and Polymeric Composites: A Reference Series*, ed. M. Mondal, Springer, Cham, 2019, pp. 789–817.

47 Z. Xia, M. Patchan, J. Maranchi and M. Trexler, Structure and relaxation in cellulose hydrogels, *J. Appl. Polym. Sci.*, 2015, **132**(24), 1–5.

48 K. Kraiwattanawong, N. Sano and H. Tamon, Influence of evaporation drying on the porous properties of carbon/carbon composite xerogels, *Polymers*, 2021, **13**(16), 2631.

49 H. Ha, K. Shanmuganathan and C. J. Ellison, Mechanically stable thermally crosslinked poly (acrylic acid)/reduced graphene oxide aerogels, *ACS Appl. Mater. Interfaces*, 2015, **7**(11), 6220–6229.

50 F. Leng, K. Robeyns and T. Leyssens, Urea as a cocrystal former—study of 3 urea based pharmaceutical cocrystals, *Pharmaceutics*, 2021, **13**(5), 671.

51 M. Z. Alvar, G. Abdeali and A. R. Bahramian, Influence of graphite nano powder on ethylene propylene diene monomer/paraffin wax phase change material composite: shape stability and thermal applications, *J. Energy Storage*, 2022, **52**, 105065.

52 G. Abdeali, K. Mazaheri, L. S. Ahmadi and A. R. Bahramian, Effect of expanded graphite surface modification on phase change materials nanocomposites thermal protection efficiency, *Polym. Compos.*, 2022, **43**(4), 1974–1984.

53 E. Gariboldi, L. P. Colombo, D. Fagiani and Z. Li, Methods to characterize effective thermal conductivity, diffusivity and thermal response in different classes of composite phase change materials, *Materials*, 2019, **12**(16), 2552.

54 A. Gounni, M. T. Mabrouk and A. Kheiri, Influence of PCMs on thermal behavior of building walls: experimental study using the walls of a reduced scale room, in *E3S Web of Conferences*, EDP Sciences, 2017, vol. 22, p. 00057.

55 T. L. Bergman, A. S. Lavine, F. P. Incropera and D. P. DeWitt, *Fundamentals of Heat and Mass Transfer*, John Wiley & Sons, 2011.

56 P. Kosky, R. Balmer, W. D. Keat and G. Wise, *Exploring Engineering: An Introduction to Engineering and Design*, Academic Press, 2015.

57 Y. O. Souci and S. Houat, Numerical study of building materials filled by PCM for thermal energy storage, *Epitoanyag*, 2018, **70**(4), 123–127.

58 X. Yang, K. Yue, D. Han and X. Zhang, Effective thermal conductivity measurement of PCM composites during phase transition by using the transient plane source method, *Mod. Phys. Lett. B*, 2022, **36**(14), 2250034.

59 Q. Nguyen, A. Naghieh, R. Kalbasi, M. Akbari, A. Karimipour and I. Tlili, Efficacy of incorporating PCMs into the commercial wall on the energy-saving annual thermal analysis, *J. Therm. Anal. Calorim.*, 2021, **143**, 2179–2187.

60 M. Song, J. Jiang, J. Zhu, Y. Zheng, Z. Yu, X. Ren and F. Jiang, Lightweight, strong, and form-stable cellulose nanofibrils phase change aerogel with high latent heat, *Carbohydr. Polym.*, 2021, **272**, 118460.

61 Y. Zhang, K. Kobayashi, Y. Teramoto and M. Wada, Preparation of cellulose-paraffin composite foams by an emulsion–gelation method using aqueous inorganic salt solution for thermal energy regulation, *Composites, Part A*, 2024, **181**, 108158.

62 X. Wei, F. Xue, X. D. Qi, J. H. Yang, Z. W. Zhou, Y. P. Yuan and Y. Wang, Photo-and electro-responsive phase change materials based on highly anisotropic microcrystalline cellulose/graphene nanoplatelet structure, *Appl. Energy*, 2019, **236**, 70–80.

63 M. Guo, P. Xu, J. Lv, C. Gong, Z. Zhang and C. Li, Engineering nanocellulose/graphene hybrid aerogel for form-stable

composite phase change materials with high phase change enthalpy for energy storage, *Diamond Relat. Mater.*, 2022, **127**, 109131.

64 H. Cui, P. Wang, H. Yang and Y. Shi, Large-scale fabrication of expanded graphite aerogel-based phase change material composite for efficient solar harvesting, *J. Energy Storage*, 2022, **56**, 105890.

65 J. Zhang, Y. Xu, X. Li, H. Li, C. Yao, S. Chen and F. Xu, Leak-free, high latent heat and self-cleaning phase change materials supported by layered cellulose/Fe3O4 skeleton for light-to-thermal energy conversion, *Energy Convers. Manage.*, 2022, **256**, 115357.

66 B. Seantier, D. Bendahou, A. Bendahou, Y. Grohens and H. Kaddami, Multi-scale cellulose based new bio-aerogel composites with thermal super-insulating and tunable mechanical properties, *Carbohydr. Polym.*, 2016, **138**, 335–348.

67 M. Kaya, Super absorbent, light, and highly flame retardant cellulose-based aerogel crosslinked with citric acid, *J. Appl. Polym. Sci.*, 2017, **134**(38), 45315.

68 G. Ferreira, S. Das, A. Rego, R. R. Silva, D. Gaspar, S. Goswami, R. N. Pereira, E. Fortunato, L. Pereira, R. Martins and S. Nandy, Eco-designed recycled newspaper for energy harvesting and pressure sensor applications, *Chem. Eng. J.*, 2024, **480**, 147995.

69 H. Takagi, A. N. Nakagaito and M. S. Bistamam, Extraction of cellulose nanofiber from waste papers and application to reinforcement in biodegradable composites, *J. Reinforc. Plast. Compos.*, 2013, **32**(20), 1542–1546.

70 D. Klemm, B. Heublein, H. P. Fink and A. Bohn, Cellulose: fascinating biopolymer and sustainable raw material, *Angew. Chem., Int. Ed.*, 2005, **44**(22), 3358–3393.

71 *Newspaper Publishing Market Size, Share, Growth – 2034*, retrieved from, **https://www.factmr.com/report/newspaper-publishing-market**, 2024 Dec.

72 *Global Printing Paper Market Size, Trends, Share 2033 – CMI*, retrieved from, **https://www.custommarketinsights.com/report/printing-paper-market**, Custom Market Insights, 2024 Oct 18.

73 R. Macwan, *Market Overview: Trends and Challenges Facing the Paper & Packing Industries*, retrieved from, **https://www.brightlysoftware.com/en-gb/blog/market-overview-trends-and-challenges-facing-paper-packing-industries**, Brightly, 2024 Oct 16.

74 *Waste Paper Recycling Market: Global Industry Analysis and Forecast (2024–2030)*, retrieved from, **https://www.maximizemarketresearch.com/market-report/global-waste-paper-recycling-market/84320**, Maximize Market Research, 2024 Aug.

75 *Alibaba Website*, retrieved from, **https://www.alibaba.com/premium/cellulose_powder_prices.html?p4phangyebuliu=1&src=sem_ggl&field=UG&from=sem_ggl&cmpgn=18084521239&adgrp=141310884398&fditm=&tgt=kwd-783495638817&locintrst=&locphyscl=1007902&mtchtyp=p&ntwrk=g&device=c&dvcmdl=&creative=617857243845&plcmnt=&plcmntcat=&aceid=&position=&gad_source=1&gclid=EAIaIQobChMI0u_92frKiwMVZJRQBh3eLiIzEAAYASAAEgKSMvD_BwE**.

76 *Sigma-Aldrich Website*, retrieved from, **https://www.sigmaaldrich.com/IE/en/search/cellulose-powder?focus=products&page=1&perpage=30&sort=relevance&term=cellulosepowder&type=product_name**.